Test of a Method for Monitoring the Geostrophic Meridional Overturning Circulation Using Only Boundary Measurements.

Chris W. Hughes *

Shane Elipot and Miguel Ángel Morales Maqueda

National Oceanography Centre, Liverpool, U.K.

John W. Loder

Fisheries and Oceans Canada, Bedford Institute of Oceanography,

Dartmouth, Nova Scotia, Canada

* *Corresponding author address:* Chris W. Hughes, National Oceanography Centre, Joseph Proudman Building, 6 Brownlow St., Liverpool, L3 5DA, U.K.

E-mail: cwh@noc.ac.uk

ABSTRACT

Measurements of ocean bottom pressure, particularly on the continental slope, make an efficient means of monitoring large-scale integrals of the ocean circulation. However, direct pressure measurements are limited to monitoring relatively short time scales (compared to the deployment period) because of problems with sensor drift. We use measurements from the northwest Atlantic continental slope, as part of the RAPID West Atlantic Variability Experiment, to demonstrate that the drift problem can be overcome by using near-boundary measurements of density and velocity to reconstruct bottom pressure differences with accuracy better than 1 cm of water (100 Pa). This accuracy permits us to measure changes in the zonally-integrated flow, below and relative to 1100 m, to an accuracy of 1 sverdrup or better. The technique employs the "stepping method"—a generalization of hydrostatic balance for sloping paths that uses geostrophic current measurements to reconstruct the horizontal component of the pressure gradient.

1. Introduction

Of the many parameters that can be measured to monitor the ocean circulation, Ocean Bottom Pressure (OBP) is one which has a number of advantages, and one great disadvantage. The most obvious advantage is the fact that it is directly related to the dominant part of the flow (outside boundary layers): the geostrophic flow. Two OBP measurements at the same depth and latitude on the continental slope, but on opposite sides of an ocean basin, will measure the zonally-integrated northward mass transport per unit depth. The integral is across the entire ocean basin at that depth. In an idealized, flat-bottomed ocean, such measurements would be thought of as sidewall pressure rather than bottom pressure. In the real ocean with sloping sidewalls, the sides are also the bottom; it is simply a matter of interpretation.

A second advantage is that of integrating right to the boundary. As a result, there is no difficulty associated with recirculations. An integral of the mass transport from the boundary to a given point in the interior may produce a highly time-dependent result simply because the interior point is at different times on either one side or another of a meandering current, or inside/outside an eddy or other local recirculation. This has the potential to result in very large, stochastic variability of little relevance to the large scale (Wunsch 2008). For example, the western boundary arrays described by Toole et al. (2011) and Schott et al. (2006), while perfectly fine on their own terms as a system for monitoring the variability within the western boundary region itself, cannot be interpreted as being representative of the zonally-integrated flow. When integrating from boundary to boundary, there is no possibility of aliasing recirculations that straddle the edge of the region, meaning that the stochastic variability will tend to be reduced.

A third advantage of OBP relates to the part it plays in the depth-integrated vorticity balance, in which it appears in the form of the bottom pressure torque. This is associated with the gradient of pressure along a depth contour on sloping topography, and hence with vertical velocities (e.g. Hughes and de Cuevas (2001)). The associated dynamical control on

OBP gradients means that gradients of OBP over a sloping boundary tend to be significantly smaller than pressure gradients in nearby interior eddies. This point will be discussed in more detail in a paper to follow, but can be thought of as a generalization of the similar boundary suppression of eddy variability discussed by Kanzow et al. (2009) for the case of an ocean with vertical sidewalls.

These points would make OBP an ideal parameter to monitor in order to measure the Meridional Overturning Circulation (MOC) were it not for one important problem: the pressure signals of interest are of order 1 cm of water equivalent, but even the best instruments are prone to drifts of order several centimetres per year or larger (Watts and Kontoyiannis 1990). However, given that we are considering an overturning circulation that, by its very nature, has a zonal integral which varies with depth, we can make progress by focusing on how the boundary pressure changes as a function of depth. In the case of a vertical sidewall, that would be particularly simple: hydrostatic balance allows us to calculate the change with depth simply from a measurement of density at the boundary, and this is the strategy used at other latitudes to measure the "interior" ocean transport between points just offshore of the continental slope (Send et al. (2011); Johns et al. (2008)). On a sloping boundary, extra information is required. On such a boundary, at constant latitude y, OBP can be thought of as a function of the horizontal zonal coordinate x, with the vertical coordinate $z = -H(x)$ being a function of x. This is the usual "looking down" viewpoint for which the sea floor is mapped onto a horizontal surface. Alternatively, we can think of OBP as a function of z, with $x = X(z)$ on that surface, taking a viewpoint in which we are effectively looking to the west at the ocean's western sidewall from a point within the ocean. Here, we map OBP onto the (y, z) plane instead of the (x, y) plane. From this point of view, we can think of how OBP varies as a function of z, but must bear in mind that as z changes, we are actually following the sloping seafloor, and so there will be an associated change in x, which will be small for steep slopes but large for gentle slopes.

This means that the vertical gradient of OBP is not simply given by the density, but also

involves the horizontal pressure gradient. For a geostrophic flow, that horizontal pressure gradient can be determined from a local current measurement. With these two measurements, density and current, it is then possible to determine how OBP changes with depth on a section across the continental slope. We have an analogue of the hydrostatic balance, but along a sloping rather than vertical boundary.

The West Atlantic Variability Experiment (WAVE) was set up as part of the RAPID experiment to demonstrate these concepts in the context of monitoring the North Atlantic MOC. In particular, an array of bottom pressure recorders, current meters and conductivity, temperature and depth (CTD) instruments were deployed in 2008 on the Canadian Atlantic continental slope at about 42–43°N, on an extension of the Halifax section (Loder et al. 2003), referred to as the RAPID-Scotian (RS) Line. In this paper, we explain the theory in more detail, present measurements from the first year of deployment, and demonstrate that variations in pressure differences over a depth range of over 2750 m can be reconstructed using density and current measurements to within 1 hPa (1 hPa = 100 Pa = 1 mbar and is approximately equivalent to 1 cm of water). Elsewhere (Elipot et al. 2012), we apply the method detailed here to investigate the coherence between signals measured at and near the RS Line, and MOC-related measurements at other latitudes. A future paper will compare observations with ocean model predictions, focusing on the suppression of eddy variability on the continental slope, and the vertical structures of observed and modeled variability.

It is worth mentioning at this point that we are focusing purely on the Eulerian MOC, by which we mean the MOC as determined by zonally-integrated transports at constant depth. To determine buoyancy or heat fluxes, one would be interested in the MOC calculated in density or temperature coordinates. At lower latitudes, where density and temperature contours are closer to horizontal, these are tightly related to the Eulerian MOC, but at the latitude we are considering there is a significant decoupling. For example the heat flux due to the horizontal "gyre" circulation can be as important as that associated with the Eulerian MOC (Marsh et al. 2009). On the other hand, the concept of "the" MOC as a large-scale,

long-period mode of circulation in the Atlantic associated with deep water formation in the north, is one that is typically associated with an Eulerian overturning streamfunction which spans the ocean from its southern limit to northern subpolar regions, and is associated with a heat transport which varies more strongly with latitude than does the flow itself, as illustrated for example in Figures 1 and 3 of Marsh et al. (2009). The version of the MOC that is of interest depends on the question being asked.

2. Theoretical development

The integral quantity we are interested in is the zonally-integrated northward mass transport per unit depth:

$$T(y,z) = \int_W^E \rho v \, dx, \tag{1}$$

where $W(y,z)$ is the x-coordinate of the western boundary of the ocean at depth z and meridional coordinate value y, and $E(y,z)$ is the corresponding x-coordinate of the eastern boundary. The coordinates (x,y,z) are in the directions (east, north, up) respectively. We will consider this integral in the light of the geostrophic relationship:

$$\rho f \mathbf{k} \times \mathbf{u_g} = \rho f(-\mathbf{i}v_g + \mathbf{j}u_g) = -\nabla_h p \tag{2}$$

where $\mathbf{u_g}$ is the geostrophic horizontal velocity, f is the Coriolis parameter, $(\mathbf{i},\mathbf{j},\mathbf{k})$ are unit vectors in the (x,y,z) directions respectively, p is pressure and ∇_h represents the horizontal gradient operator. A zonal integral of the zonal component of (2) then leads to

$$T_g(y,z) = \int_W^E \rho v_g \, dx = \frac{p_E(y,z) - p_W(y,z)}{f}, \tag{3}$$

where T_g is the geostrophic component of T, and p_E and p_W are OBP at the eastern and western boundaries respectively. Thus, as long as the geostrophic transport dominates, the net northward transport at each depth is determined simply by the difference between eastern and western boundary pressures at a given depth and latitude. As shown in an ocean model

context by Bingham and Hughes (2008), this does indeed appear to be the case over most of the ocean depth, with the near-surface Ekman layer as the most obvious exception.

Since we are interested in the overturning component of the circulation, it is helpful to decompose the transport as follows:

$$T(y,z) = T_g(y,z) + T_{Ek}(y,z) = T_0(y) + T_c(y) + T_d(y,z) + T_{Ek}(y,z). \tag{4}$$

Here, $T_{Ek}(y,z)$ represents the zonal integral of all ageostrophic mass transports, which we assume are dominated by the wind-driven near-surface Ekman transport. This can be diagnosed from the wind stress alone, along with an assumption of its distribution within a near-surface layer. All other terms are therefore geostrophic, and sum to give $T_g(y,z)$. T_c (subscript c stands for compensation) is a depth-independent geostrophic term chosen to compensate T_{Ek} in a vertical integral. Thus, $T_c + T_{Ek}$ represents an overturning circulation in which a near surface southward flow is balanced by a geostrophic northward return flow for which the zonal integral is independent of depth. This is not supposed to be physically correct; the real return flow will be distributed over a range of depths. It is simply a mathematical device that conveniently allows us to separate out the part of the geostrophic flow for which the zonal integral depends on depth.

The term T_0 is a constant, independent of depth, chosen such that $T_0 H_{\max} = Q$, where $H_{\max}$ is the maximum ocean depth at that latitude, and Q is the net northward mass transport across the latitude (a term often assumed to be zero, though it is not exactly so; in the Atlantic it includes the recirculation from the Pacific through the Bering Strait, as well as terms associated with mass sources and sinks, and accumulation of mass north of the chosen latitude). In other words, T_0 accounts for the net northward mass transport in a way that introduces no depth dependence, and is therefore irrelevant to the overturning component of the flow.

With these definitions, the depth-averaged geostrophic transport is $T_0 + T_c$, which leaves the term $T_d(y,z)$ to represent departures of the zonally-integrated geostrophic transport from its depth average (subscript d stands for depth-dependent; by definition, the depth-integral

of T_d is zero). Taking the vertical derivative of (3), we find that

$$\frac{\partial}{\partial z}T_g(y,z) = \frac{\partial}{\partial z}T_d(y,z) = \frac{1}{f}\frac{\partial}{\partial z}\left[p_E(y,z) - p_W(y,z)\right]. \tag{5}$$

Given the constraint that the depth integral of $T_d(y,z)$ is zero, this implies that all we need to determine this component of the overturning circulation is $\partial/\partial z$ of the boundary pressure terms p_W and p_E. For the case in which the net northward transport T_0 is known, this separation into depth-dependent and depth independent components represents a means of determining the "reference level transport" in this analogue of a thermal wind balance calculation. In the case of an ocean with vertical sidewalls, this is particularly simple as the hydrostatic balance equation can be used:

$$\frac{\partial p}{\partial z} = -\rho g. \tag{6}$$

When (as in reality) the ocean has sloping sidewalls, there are two approaches that can be taken. Use of the hydrostatic equation can be retained by defining a vertical-walled box within the ocean and calculating transports within this box, as is done within the RAPID-MOC array at 26°N (Rayner et al. 2011). In this case, there will be roughly triangular regions between the box and the sloping ocean walls that must be measured directly, with current meters for example, to complete the integral across the entire basin. The alternative, which we focus on here, is to continue to integrate across the entire basin, and to generalize the hydrostatic equation to work along lines that are not vertical. We do this by combining the hydrostatic equation (6) with the geostrophic relationship (2) to give an equation for the three-dimensional pressure gradient:

$$\nabla p = -\mathbf{k}\times(\rho f \mathbf{u}_g) - \mathbf{k}\rho g = \rho(\mathbf{i}v_g f - \mathbf{j}u_g f - \mathbf{k}g). \tag{7}$$

We can treat this relationship as a generalization of hydrostatic balance that allows the computation of pressure differences between any two points, c and a, rather than just points that are immediately above or below each other:

$$p_c - p_a = -\int_a^c \left[\mathbf{k}\times(\rho f \mathbf{u}_g) + \mathbf{k}\rho g\right]\cdot d\mathbf{s} = \int_a^c \rho f u_L \, ds - \int_{z_a}^{z_c} \rho g \, dz, \tag{8}$$

where $d\mathbf{s}$ is the three-dimensional differential vector along the path of the integral, ds is the infinitesimal *horizontal* distance along the line of the integral (in the case of a path at constant latitude it would be dx) and u_L is the velocity directed to the left of that line (to the north, in the case of integrating in the positive x direction along a constant latitude line).

In the case where the integral is performed along (or just above) the sea floor, defined as $z = -H(x, y)$, we can write $ds = -dz/H_s$ where $H_s = \partial H/\partial s$, so that (8) becomes

$$p_c - p_a = -\int_{z_a}^{z_c} \left(\frac{\rho f u_L}{H_s} + \rho g \right) dz. \tag{9}$$

This is a very simple principle. For a small separation between a and c, it can be thought of as using geostrophic balance to calculate (from the current) the horizontal pressure difference between a and c' (a point vertically above c but at the same depth as a), followed by using hydrostatic balance to determine the pressure difference between c' and c.

Differentiating (9) with respect to z then gives

$$\frac{\partial p_b}{\partial z} = -\frac{\rho f u_L}{H_s} - \rho g, \tag{10}$$

which applies along a path on the sea floor (subscript b represents a value at the sea floor). This is the crucial relationship that allows us to infer gradients of boundary pressure from boundary measurements of density and current alone.

This is clearly a generalization of the hydrostatic relation for a sloping path. For the case in which the horizontal component of that path is zonal, u_L becomes v at the bottom and H_s becomes H_x, which, in combination with (5), gives

$$f \frac{\partial T_g}{\partial z} = g(\rho_W - \rho_E) + \left(\frac{\rho f v}{H_x} \right)_W - \left(\frac{\rho f v}{H_x} \right)_E. \tag{11}$$

For practical use, it is worth commenting that the density that appears in the hydrostatic part of (10) (ρg), and related equations can be replaced by a density anomaly (i.e. difference of density relative to a reference vertical profile, $\rho' = \rho - \rho_r(z)$) as long as pressure is to be considered as the difference from the corresponding hydrostatic reference profile

($p' = p - p_r(z)$). However, wherever the density appears multiplying velocity, it must at least approximate the full density. In the case of an ocean model that uses the Boussinesq approximation, setting density to a constant ρ_0 in the momentum equation, then ρ_0 should be used to multiply velocity wherever the combination ρu, ρv, or ρw, occurs: in the horizontal momentum balance, and in (1), the definition of T. With such a convention, it becomes reasonable to separate the total $z-$dependent transport into contributions associated with density anomaly and current values at the eastern and western boundaries independently. Thus, $T_d = T_E + T_W$, and we can write

$$fT_E(y,z) = p'_E(y,z) + C_E(y) \qquad fT_W(y,z) = -p'_w(y,z) + C_W(y) \tag{12}$$

where C_E and C_W are constants at each latitude chosen so that T_E and T_W each integrate to zero over the ocean depth, ensuring that each represents an overturning. With that constraint, any constant in the definition of the reference pressure profile becomes irrelevant, so all that needs to be specified is a reference density profile, which implies the pressure (apart from a constant) via hydrostatic balance. For present purposes we will, in concept, assume a time-independent reference density based on an average taken over an area of deep water towards the eastern side of the ocean basin, though this could in principle be a time-dependent profile (in practice, as we are here only looking at departures from a time average, the assumed reference profile plays no role). With this assumption, we can allocate components of the overturning circulation to the western and eastern boundaries separately, although this separation does not imply that the flows contributing to the transport must be concentrated near either boundary. Accompanying this decomposition, we must use the correspondingly-modified version of the generalized hydrostatic equation:

$$\frac{\partial p'_b}{\partial z} = -\frac{\rho f u_L}{H_s} - \rho' g. \tag{13}$$

This modified form of (10) is the form we will use for calculations in Section 4.

The relative importance of the velocity and density terms in (13) clearly depends on how steep the slope is, as the relationship reverts to hydrostatic balance when the path becomes

vertical and H_s becomes infinite. As an indication of the size of current needed, consider a circulation in which T_d (the depth-dependent part of the zonally-integrated geostrophic northward mass transport) is constant above 500 m depth, and then reduces linearly from a northward value $T_s = 10^6$ kg m^{-1}s^{-1} (approximately equivalent to one sverdrup per kilometre of depth) to zero, over 1000 m of depth. This gives a net northward transport above 1500 m of approximately 1 Sv and, below 500 m, $T_z = \partial T_d/\partial z = 1000$ kg m^{-2}s^{-1}. Assuming this is entirely due to the velocity term on the western boundary, rather than the density, this requires a bottom current given by $v = H_x T_z/\rho$ which, for $\rho = 1000$ kg m^{-3} leads to $v = 1.0$ m s^{-1} $\times$ H_x, meaning that a 1 Sv overturning would require 10 cm s^{-1} bottom currents on a slope of 0.1, or 1 cm s^{-1} on a slope of 0.01. For reference, the continental slope at the RS Line has a slope of about 0.05, reducing to 0.01 at the foot of the slope (Fig. 1). There is no practical difficulty in measuring currents to this accuracy, the only questions are whether they can be measured with sufficient spatial resolution, and whether the measured currents are sufficiently close to geostrophic for (13) to be used.

In comparison, in the case of the RAPID-MOC array at 26°N, the eastern continental slope is rather gentle, with a typical slope of only about 0.02, and less below about 3000 m. However, the western continental slope is extremely steep with an average slope between 1500 m and 4000 m depths of about 0.35, and significantly steeper over some depth ranges (Rayner et al. 2011), reducing the relative contribution of currents to the boundary pressure gradient. In fact the WB2 mooring, in almost 4000 m depth, is only about 7 km horizontally from the 1500 m depth contour. The MOC calculation at 26°N, which relies on performing a thermal wind calculation for an interior box-like ocean and then measuring currents to the west of that box, is effectively the same as calculating the vertical gradient of boundary pressure from the hydrostatic pressure gradient at WB2, extended to the western boundary using horizontal pressure gradients inferred from the currents. Seen purely from the point of view of determining the Eulerian MOC, parts of the 26°N array are thus redundant. From a wider perspective, these redundant parts add information about the local current structure

and water mass properties, and can improve the calculation of heat and buoyancy fluxes by accounting for correlations between currents and departures of temperature and density contours from the horizontal. The lack of current measurements on the gently-sloping eastern boundary array calls into question the determination of the eastern boundary contribution to total MOC variability on time scales for which currents contribute to this, although the eastern contribution is generally expected to be smaller than the western contribution.

The accuracy required of density measurements is given by assuming that the same vertical pressure gradient that was assumed above to result from currents, instead results from the density anomaly in (13), i.e. $1000\ \mathrm{kg\,m^{-2}s^{-1}} = \rho' g/f$. Taking $g/f = 10^5\ \mathrm{m\ s^{-1}}$ (which, coincidentally, is exactly true at a latitude lying within the RS Line) leads to an equivalent accuracy requirement for ρ' of $0.01\ \mathrm{kg\,m^{-3}}$. This level of accuracy is attainable, although very careful calibration is needed to improve substantially upon this level. Thus, for slopes steeper than about 0.01, it is likely to be the accuracy of the density measurement that is the limiting factor if significant density variations occur and spatial sampling is sufficient.

Note that the presence of currents as well as density in (13) means that there is no need for the flow to have a vertical shear of the current in order to produce a vertical shear in the zonally-integrated transport T. This is simple to understand: consider an ocean basin that is 4 km deep everywhere except in a region near the western boundary, where it is 1 km deep. If a depth-independent flow is to the north in the shallow region and to the south in the deep region (compensating each other so that there is no net northward mass transport), then T must be to the south at any depth below 1 km and, because it must integrate to zero, must be to the north at depths above that. There is therefore an overturning circulation with no vertical shear in the velocity.

With this in mind, it clearly does not make sense to refer to T_d as a baroclinic transport and T_0 and T_c as barotropic, although T_d has no depth integral and T_0 and T_c have no depth dependence. For that reason, we refer to T_d as an overturning transport. Other concepts familiar from thermal wind calculations remain valid, such as the concept of a flow

(in this case a zonally-integrated transport) measured relative to an assumed depth of no (zonally-integrated) motion, but such a flow need not be baroclinic in nature.

3. Measurements on the RAPID-Scotian Line

The fourth deployment of the WAVE experiment (the first with a suite of current and density measurements) under the NERC-funded RAPID-WATCH programme took place on October 2 and 3, 2008, during the *CCGS Hudson* expedition 2008-037, under a collaboration between the UK National Oceanography Centre and the Canadian Bedford Institute of Oceanography. The RS array, consisting of 5 short moorings (RS1 to RS5) and one tall mooring (RS6), was deployed across the Scotian continental slope between approximately 1100 and 3900 m water depth (Figs. 1 and 2; Table 1). Each short mooring (approximately 100 m length) was equipped with a Seabird 53 Bottom Pressure Recorder (BPR) on its anchor, an upward-oriented 120-m nominal range RD Instruments Workhorse 300 kHz Acoustic Doppler Current Profiler (ADCP) mounted 50 m above the anchor and, a further 50 m above, a Seabird SBE37 (MicroCAT) temperature/conductivity/pressure recorder. The tall mooring RS6 (3000 m length) had the same configuration at its bottom but included 5 additional MicroCATs mounted at approximately the same depths as the MicroCATs on the short moorings up the slope.

From the nearby Line B, described in Elipot et al. (2012), earlier near-bottom temperature measurements had shown that temperature variations are highly coherent throughout the range 100 to 500 m above the bottom, but temperatures at the bottom are somewhat different. This implies a bottom boundary layer of less than 100 m thickness, consistent with the more general findings of Lozovatsky and Shapovalov (2012).

Recovery and re-deployment of the moorings took place during the Hudson expedition 2009-048, between September 26 and 30, 2009. All instruments returned data except the ADCP at RS5, which was flooded. Table 1 provides a summary of location, water depth,

and instrumental record length of each mooring.

With these measurements, we have the information necessary to assess whether downslope pressure gradients can be reconstructed accurately from current and density measurements as given by (13). The left-hand side of this equation, the pressure differences, are obtained from the BPR data. Such data always suffer from drifts (Watts and Kontoyiannis 1990) and the impossibility of determining absolute pressure and depth to the subcentimeter accuracy required. In addition, the assumption of geostrophic balance cannot be expected to hold at periods shorter than about a day. For these reasons, we focus on versions of the time series that have been filtered to pass periods between 1 and 50 days (from spectral analysis of pressure difference time series with and without removal of drifts, the effect of drift dominates at periods longer than about 50 days). As we show below, the resulting time series compare well with the reconstructions from velocity and density data.

a. Bottom pressure estimates from BPR measurements

The manufacturer's calibrations were applied to the BPR data, which were sampled as 5-minute averages every 20 minutes. High frequency tides were removed by least-squares fitting of 97 tidal components with periods of 28.0062 hours (2Q1) and shorter. There is too much power near the periods of the fortnightly and monthly tides for a reliable estimate of these to be made from the data (expected amplitudes of these tides are below 1 hPa), so these tides remain in the records but are not expected to change by much across the array. Pressure differences at these longer periods should in any case be close to geostrophic balance, and should therefore also appear in the currents.

Intercomparison of the tidal residuals (Fig. 3) showed that five of the six datasets had drifts compatible with the expected exponential plus linear function of time as described by Watts and Kontoyiannis (1990). The exception was RS3 which, in comparison with the average of RS2 and RS4, showed 4 short periods of disruption producing steps in the record, each of which appeared to initiate a new exponential adjustment phase with approximately

the same amplitude and time constant. If the steps had resulted from a movement of the instrument, we would not expect such exponential adjustments given that the steps are only of order 10–20 hPa, smaller than the tidal amplitude (we cannot use the density or current measurements to check for such a small instrument movement, although it is clear from the current measurements that there was no significant rotation of the instrument). The comparison in Section 4 shows that the jumps and exponentials can not be genuine signals. Thus we assume the disturbances to be instrumental errors perhaps associated with anomalous behaviour of the quartz crystal. Steps plus exponentials were added following each event, the latter each having an amplitude of 1.5 hPa and time constant of 200 time steps, or 66 hours and 40 minutes. While this procedure brought the variability at RS3 into line with the other records, the resulting time series should be treated with caution.

Following the special treatment of RS3, a composite record was formed from the average of all six time series, and a linear trend removed from the composite. Exponential plus linear trends were then fitted to the differences of each record from the composite record. The initial (detided) timeseries, overall fitted trends, and final residuals are plotted in Fig. 3. The residual time series are clearly dominated by a highly coherent mode, although additional variability is also apparent at RS6. This is also clear from the standard deviations, which increase gradually from 2.46 hPa at RS1 to 2.57 hPa at RS5, and then jump to 3.01 hPa at RS6. In an attempt to reduce trends from clock drift, a reference clock comparison was available every 7 days, but the observed trend amplitude was typically about ten times larger than could be accounted for from this source (and the jumps in RS3 were not explained by the comparison), so information from the reference clock was not used further.

Figure 4 shows the difference between neighboring pairs of residual pressures. The differences clearly have a spectrum that is different from the full pressure, and also show a degree of coherence between depths, with RS6 once again standing out as introducing extra variability (with some also at RS5). These timeseries have standard deviations of between 0.67 and 0.9 hPa except for RS6-RS5, which has a standard deviation of 2.1 hPa.

b. Velocity estimates from ADCP measurements

The ADCPs were configured to have hourly sampling, and their depth bins were centered at 4 m range intervals, with the first bin centered on 6.1 m and the 30th bin centered on 122.1 m above the instrument. Hourly current directions in each bin were rotated into an earth-fixed coordinate system using the magnetic compass of the instrument, corrected for the local magnetic declination. A time-dependent magnetic declination correction was obtained from the Magnetic Field Calculator of the USA National Geophysical Data Center (approximately -18° at these locations and times). The data from the first bin of each ADCP were degraded and hence discarded. The data were processed using the RD Instrument processing software, with standard error thresholds used to determine which bins were returning good data. The usable range varied with time and mooring, with the last usable bin being bin 30 for RS1, between 23 and 30 for RS2, between 17 and 30 for RS3, and between 11 and 29 for both RS4 and RS6.

An inspection of the velocity time series in each bin revealed that currents are very strongly correlated in the vertical, and almost independent of depth between bins 2 and 8 or 9. For a few bins either side of the depth of the MicroCAT instrument mounted on each mooring (approximately 50 m above the ADCP), velocities appeared to be biased low, but beyond the MicroCAT an increase in velocity was seen. In order to avoid any question of tuning the data to match the pressure observations, we simply considered the velocity averaged over all bins considered to be good at any time. Tests using an alternative average over bins 2–8 or 2–9 produced insignificant differences in the pressure reconstructions reported in Section 4.

The principal components of the resulting velocity time series at each mooring are plotted in Fig. 5, with the corresponding variance ellipses plotted in Fig. 6. For display purpose only, these series have been filtered by a 3rd order Chebyshev low-pass filter with 0.5 decibel peak-to-peak ripple in the passband, with a frequency cut-off of 1 cycle per day.

Generally, the flow across depth contours is suppressed compared to that along the con-

tours, especially at longer periods. Like the pressure differences, the along-slope flow fluctuations are coherent from one site to the next, but greater variability is seen at the deepest site (RS6).

c. Density estimates and their errors

The MicroCAT datasets (with sampling every 10 minutes) are of very high quality for temperature and conductivity but exhibit some significant drifts and offsets for their pressure records, which can be important for the computation of in-situ density. The on-board calibration procedure described in Kanzow et al. (2006) was applied to each instrument, during both deployment and recovery cruises. This process involves taking collocated measurements with both MicroCATs and shipboard CTD, which was in turn carefully calibrated against bottle samples by Igor Yashayaev (Bedford Institute of Oceanography).

Our best values, used here, use calibration coefficients interpolated linearly in time between the values determined at deployment and recovery of the instruments. The root mean square differences between the pre- and post-calibrated temperature, conductivity and pressure of the MicroCATs are on average 1.1×10^{-3} K, 2.1×10^{-4} S m^{-1} and 4.5 dbar. These values are consistent with the expected errors provided by the manufacturer. Salinity was computed from the calibrated temperature, conductivity, and pressure, and then de-spiked based on a threshold value of the second-order time derivative.

Roughly (to better than a factor of two depending on water properties), errors of the size noted above imply a salinity-induced density error of 0.004 kg m^{-3}, and hence a pressure error of 40 Pa km^{-1}, and a temperature-induced error of 2 Pa km^{-1}. The pressure uncertainty of 45 kPa (equivalent to approximately 4.5 m uncertainty in depth) produces a density error of about 0.02 kg m^{-3}, which would give a larger error of about 200 Pa km^{-1}. However, that is an overestimate of the effect of pressure errors in our calculation. We are only concerned with the density difference between two points at the same, constant depth. Excluding tidal variability, Fig. 3 shows that such points will always be at the same pressure to within 2 kPa

or so, about a factor of twenty smaller than the 45 kPa uncertainty in pressure measured on the MicroCAT. Thus, the relevant pressure-related uncertainty is about twenty times smaller than 200 $\mathrm{Pa\,km^{-1}}$, giving 10 $\mathrm{Pa\,km^{-1}}$. We simply have to ensure that density is always calculated as difference from a reference density calculated at the same pressure. To this end, the densities we use are calculated at a constant pressure for each site, corresponding to the time-average of the pressure measured by the BPR.

Consistent with the above error estimates, the difference in densities calculated using the pre-calibration temperature and salinity and our final product (both at the same standard pressure) has a standard deviation of between 0.0011 and 0.0055 kg $\mathrm{m^{-3}}$ for the six sites. The calibrated data should be better and, in an attempt to assess how much better, we have calculated differences between densities using either the two different calibrations (pre-deployment and post-deployment), and our final product, which interpolates in time between the two calibrations. These give standard deviations between 0.0015 and 0.0026 kg $\mathrm{m^{-3}}$, leading to pressure errors of 15 to 26 $\mathrm{Pa\,km^{-1}}$. Smaller errors would be appropriate if the linear drift in calibration is a good model, but it is worth noting that these errors (dominated by the salinity term) are not completely negligible in comparison to the 100 $\mathrm{Pa\,km^{-1}}$ signal produced in our example case of 1 Sv overturning. Exactly the same errors are incurred in a conventional thermal wind calculation using a vertical mooring.

Figure 7 shows the 10-min interval time series of in-situ density anomalies. For display purposes, lowpassed versions of each time series, using the same filter as for the velocity time series, are also shown. For comparison, the in-situ density anomalies estimated from the RS6 mooring data at similar pressure levels are also shown in Fig. 7b. Note the substantial differences between these time series and the near-bottom time series at the equivalent depths, especially for the shallower data.

d. Expected errors due to the geostrophic assumption

The development so far has been based on the assumption that the horizontal flow is geostrophic. In the bottom boundary layer, this can be upset by turbulent viscosity but, as noted above, we believe our measurements to be outside the boundary layer. However, there are other ageostrophic terms that can upset the assumed balance. The size of these can be assessed by extending (2) to include time-dependent and nonlinear terms:

$$\frac{\partial \mathbf{u}}{\partial t} + (f+\zeta)\mathbf{k}\times\mathbf{u} + w\frac{\partial \mathbf{u}}{\partial z} = -\left(\frac{\nabla_h p}{\rho} + \frac{\nabla_h(\mathbf{u}\cdot\mathbf{u})}{2}\right), \tag{14}$$

where ζ is the vertical component of the relative vorticity.

The relative size of the ageostrophic terms can be assessed by comparing them with the geostrophic terms of size $f\mathbf{u}$ and $(\nabla_h p)/\rho$. The first, time-dependent term is smaller than $f\mathbf{u}$ by a factor ω/f where ω is the angular frequency of the oscillations in velocity. At the latitude of the array, this ratio is 1 at a period of 0.73 days, reducing to 0.1 at 7.3 days, and so on, so we can expect strong deviations from geostrophy at periods of a few days and shorter.

The size of the first nonlinear term can be assessed from the ratio ζ/f, with a scale for ζ given by V/L where V is a change in along-slope velocity over a length scale L. From Fig. 5, a typical velocity is 0.05 m s^{-1} and a large velocity is 0.1 m s^{-1}, except at RS5 where the extreme velocity reaches about 0.3 m s^{-1} and 0.1 m s^{-1} might be considered typical. The horizontal separation between measurements is typically about 10 km, and the coherence between measurements at different depths means that the relevant velocity difference V will be smaller than the total velocity. Thus, taking $V = 0.05$ m s^{-1}, $L = 10$ km, and $f = 10^{-4}$ s^{-1}, we obtain a ratio $\zeta/f = 0.05$, with slightly larger values expected at RS6, meaning the flow should be comfortably within 10% of geostrophy except perhaps at the deepest station.

The fractional disturbance to geostrophy from the second nonlinear term is wu_z/fv, where $u_z = \partial u/\partial z$ and u is the downslope velocity component. We can estimate the size of w from us where s is the slope (about 0.05), and make an overestimate of u_z as u/h with

$h = 50$ m (this assumes that the vertical shear produces an order (1) change to the flow over 50 m, larger than we see in the ADCP data which usually has rather little shear in the first 50 m). Using these estimates leads to $wu_z/fv < u^2 s/fvh$, and writing $u = \beta v$, then substituting numerical values for s, f and h, gives $wu_z/fv < 10\beta^2 v$ with v in m s^{-1}. With along-slope velocities typically more than three times larger than cross-slope velocities (Figs. 5 and 6), this results in $wu_z/fv < v$(m s^{-1}). This gives an upper bound on the effect of the second nonlinear term, which is similar in size to the first.

The size of the third nonlinear term (on the right hand side of the equation) is best expressed by comparing it directly with a pressure signal. The size of the perturbation to the pressure is thus given by $\rho U^2/2$, where U now is the total velocity. Choosing $U = 0.1$ m s^{-1}, this gives a value of 5 Pa, equivalent to 0.5 mm of water. This is an upper limit for RS1–RS4, and the quadratic dependence on U means that the effect will usually be substantially smaller. At RS6, the occasional extreme value of about 0.3 m s^{-1} leads to a ten times larger perturbation of around 50 Pa, or 5 mm of water.

Taken together, these scalings suggest that the dynamical balance we observe should be within 10% of geostrophy at periods longer than about 14 days, with perhaps larger departures up to about 5 mm of water (50 Pa) at the deepest site. This is an assessment of the dynamical error, independent of instrumental or sampling errors.

4. Test of the stepping method

The generalized hydrostatic relationship (13) allows us to use measurements of density and currents to calculate pressure differences between two sites on the continental slope. We refer to the use of this equation as the "stepping method". With the reality of discrete measurements at six sites, this allows us to calculate five steps in pressure, and questions arise about how best to perform these discrete steps. These are addressed in the Appendix, in which we derive three different methods. Method 1, using Equation (A10), effectively

assumes that currents should be linearly interpolated between measurement sites. Method 2, using Equation (A12), assumes that the flow is strongly steered by topography, and the dominant interpolation error results from the fact that the topographic gradient is not constant between measurements. Method 2e, using Equation (A16), is an extension of Method 2 that also accounts for cross-slope flows on the assumption that these are not a source of noise for the geostrophic calculation.

Density and pressure data are available for all sites, but no currents are available from RS5 (Table 1). In order to be able to use the stepping method at all depths, we calculated a synthetic velocity time series for RS5 based on a linear combination of lagged velocities at RS4 and RS6, with lags and coefficients chosen so as to produce the best agreement between the RS4–RS5 directly-measured pressure difference time series and that produced by the stepping method. Thus

$$v_5(t) = a_4 v_4(t - \tau_4) + a_6 v_6(t - \tau_6) \tag{15}$$

where the optimal parameters for Method (1,2) are $a_4 = (0.58, 0.60)$, $a_6 = (0.26, 0.24)$, $\tau_4 = (2.45, 2.58)$ days, and $\tau_6 = (-3.85, -3.82)$ days, implying a signal that propagates down the slope with time.

This is the only case for which any tuning has been applied. A degree of confidence in the reconstructed velocity is obtained from the fact that it does not noticeably degrade the fit for the independent RS5–RS6 step, and in fact improves the skill from 0.45 to 0.58 in the case of Method 1, as compared to a reconstruction using weighted RS6 velocity only. We define skill as the fraction of variance of the measured pressure difference explained by the stepping method, without any scaling applied. Mathematically, skill is defined as

$$1 - \left\langle (\delta p - \delta q)^2 \right\rangle / \left\langle \delta p^2 \right\rangle , \tag{16}$$

where $<>$ represents a time average, δp is the directly-measured pressure difference between two sites, minus its time average, and δq is the pressure difference between two sites reconstructed from density and current measurements, minus its time average.

With this tuning for RS5 velocity, and the doubts discussed above for the RS3 ocean bottom pressure (OBP), that leaves us with two completely "clean" cases to test. The RS1–RS2 step has complete information, and we can also compare the RS2–RS4 pressure difference with the sum of the two steps from RS2–RS3 and RS3–RS4. For these steps, the directly-measured pressure differences and reconstructions using Method 1 are illustrated in Figs. 8 and 9. Note that we use the convention of plotting deeper minus shallower pressure and, for time series plots and statistics quoted, we apply a 1–50 day band-pass filter because geostrophy can only hold at periods longer than the inertial period (0.74 days), and the power in the OBP drift correction becomes dominant at longer periods. We also ignore the first month of observations because of apparent remaining drifts in the BPR records, despite the detrending applied to the data.

Figures 8 and 9 tell us a number of things. The reconstruction is very good, particularly (as expected) at periods long compared to the inertial period. Both velocity and density contribute to the reconstruction, with the density contribution being smaller but increasing in relative size at longer periods (there is a noticeable improvement in phase agreement when the density contribution is included). There is a strong dip in the squared coherence at about 0.2 cycles per day (5-day period), and a weaker dip around 0.09 cycles per day (11-day period). The causes of these dips are not known, but they are seen for all pairs of sites (not shown), and suggest an ageostrophic mode of variability at these frequencies.

The quality of the reconstruction for all neighboring pairs of instruments is shown in Table 2. Errors are typically 20–30 Pa, except in the poorly-sampled deepest region for which some velocity data are missing. In Section 3c, we estimated a measurement error dominated by salinity calibration errors of about 20 $\mathrm{Pa\,km^{-1}}$, which translates to 10 Pa over the approximately 500 m steps here. The reconstruction includes three further sources of error: sampling error, representation error, and errors in the BPR data. Sampling error relates to the spatial resolution of the measurements and the question of whether the necessary interpolation is adequate; representation error relates to the question of whether

the pressure gradients are sufficiently close to geostrophic and hydrostatic balance with the measured current and density respectively. The fact that the total error is comparable to the estimated measurement error shows that neither sampling nor representation error is overwhelmingly large compared to measurement error.

Based on the skills and errors in Table 2, we cannot say whether Method 1 or Method 2 is better. Method 2e is systematically (though not significantly) worse than Method 2, except at RS5–RS6 where Method 1 clearly does best. This reflects the fact that the measured velocities are highly correlated between neighboring sites, again suggesting that they are well resolved, except at the deepest sites where data are missing and where the variability in pressure differences rises rapidly between sites. As we saw in Fig. 4, extra variability is introduced below RS5, where the continental slope becomes less steep. This, coupled with the missing velocity data from RS5 results in a significantly degraded reconstruction at RS6.

It is also noteworthy that, although density alone accounts for only a small part of the variance (it actually has negative skill for RS1–RS2), addition of the density contribution to the velocity contribution typically increases the skill from about 0.6 to 0.8 (again, with the exception of steps involving RS5, and higher for the cases excluding the dubious pressure record at RS3). Again we see that density is making an important contribution, although the dominant signal is due to velocity.

The aim of the method is to determine pressure anomalies relative to a particular reference depth. Accordingly, the quantity of interest is the pressure difference relative to RS1, which is shown in Fig. 10. Table 3 lists, for Method 1 and Method 2, the skills and remaining errors for such pairs. Excluding the final step to RS6, the stepping method explains between 84% and 92% of the variance in each time series, with total error rising gradually with depth to about 50 Pa, and jumping to about 100 Pa at RS6.

Using this pressure field to calculate T_W, the western contribution to the zonally-integrated geostrophic transport from (12), and linearly interpolating these transports between measurement depths, we can integrate up the implied meridional transport below and relative to

the depth of RS1. This results in standard deviations of total transport integrated between RS1 and (RS4, RS5, RS6) respectively of (0.98, 1.87, 2.56) Sv based on BPR data, and (0.91, 1.77, 2.50) Sv based on the stepping method. The corresponding difference time series have standard deviations of (0.32, 0.56, 0.82) Sv, and these numbers serve as error estimates for the transport determinations (data from October 2008 are not used in determining these figures, as the initial transient in the BPR data remains significant over this period). Note that these transport measurements are, strictly-speaking, mass transports measured in units of Mts^{-1} (megatonnes per second), equivalent to sverdrups for a density of 1000 kgm^{-3}. Using the true density changes the numbers by a few percent and adds a similarly-sized depth dependence, which only serves to confuse interpretation as it is mass, not volume, which is the conserved quantity.

The above figures are based on bandpass filtered time series, which pass a longest period of 50 days, as plotted in Fig. 10a. This long period limit was imposed by limitations of the BPR measurements, but those limitations do not apply to the stepping method, as density and velocity measurements suffer from much lower long period errors. Accordingly, in Fig. 10b we plot the same quantity, but with a low-pass filter applied that passes all periods longer than 1 day. The grey line in this figure shows the density contribution to these total pressure time series. Standard deviations of transports integrated from RS1 to (RS4, RS5, RS6) are increased to (1.28, 2.45, 3.49) Sv, with the density contribution to transport producing standard deviations of (0.81, 1.45, 1.99) Sv.

The density contribution is again seen to contribute significantly, especially at the longest time scales, although the contribution resulting from currents clearly dominates. Most importantly, repeated deployments of the array, which would introduce unknown offsets in the directly-measured pressure time series, will introduce much smaller calibration errors via the stepping method. This means that it will be possible using later deployments to produce a time series capable of resolving interannual variability in the transports.

Finally, we revisit the question of trends in the BPR data. The detrending described

in Section 3a used only BPR data, in order to ensure that comparisons were between independent datasets. However, once the stepping method is accepted, it provides a means to improve the choice of detrending. Given that the stepping method only provides a measure of pressure differences, it clearly cannot resolve separate linear trends for each BPR, as the same trend could be added to each time series without appearing in the differences. The situation is, in principle, different for the exponential part of the trend: if different exponentials have different time constants, then a fit of N exponentials (one for each pressure time series) to $N-1$ time series of pressure differences could be possible. In practice, however, we find that such a simultaneous fit is unstable and produces very little reduction of residuals beyond the simpler method we describe here.

We assume that the error in pressure from one measurement is a purely linear trend (here we choose RS1, though choosing RS2 instead produces very similar results). In Fig. 11 we show, for RS2, RS4 and RS5, the difference in pressure time series relative to RS1, after subtracting the dynamical signal as determined by the stepping method, but with no detrending applied to the BPR measurements. The fitted exponential plus linear trends clearly do a good job of explaining these instrumental errors, and there is rather little large-scale structure to the final residuals after subtracting these fitted trends, shown in the lower panel. There remain hints of larger residuals in the first few weeks of the time series, and the exact time constants of the fitted exponentials do vary somewhat depending on which instrument is chosen to have a constant trend. We also tried an iterative fitting method, in which an exponential plus linear trend was found for RS1 after fitting trends to the other time series, with this repeated starting with the new, detrended version of RS1 each time. This produced a very long time constant for RS1, effectively equivalent to fitting a quadratic trend, but it reduced the final residuals by only a very small amount.

The final residual variability noted on Fig. 11 is very similar to the values given in Table 3, despite including additional variability at periods longer than 50 days. There is certainly no structure in the final residuals in Fig. 11 of sufficient amplitude to justify the investigation of

other forms of detrending function, though it is quite apparent that detrending is necessary, and that the functional form must involve monotonic curvature concentrated towards the start of the time series, as provided for by the exponential plus linear form.

5. Summary and conclusions

For a box-like ocean with vertical sidewalls, the application of thermal wind balance together with density measurements at the eastern and western boundary of the ocean makes it possible to determine the geostrophic component of the MOC at a given latitude. In the real ocean, with sloping sidewalls, additional information is needed. Rather than follow the path of splitting the ocean into a box-like interior region, for which thermal wind can be used, and a separate slope region that must be measured separately, we demonstrate how the thermal wind concept can be extended to apply to integrals over more complex domains. This uses a generalization of hydrostatic balance for paths that are not vertical, given by (13), and shows how the geostrophic component of the MOC can be computed based on measurement of boundary values only. This requires, in addition to density measurements, measurements of the near-bottom current. Simple scale analysis shows that, for typical continental slope steepness, the accuracy required of current measurements (of order 1 cm s^{-1}) is well within the capability of available instruments.

For the period October 2008 to September 2009, as part of the RAPID-WAVE experiment, we deployed instruments at six sites on the northwest Atlantic continental slope off Halifax, Nova Scotia, covering the depth range from approximately 1100 m to 3900 m. With the data from these instruments, we were able to compute this generalization of the hydrostatic balance at the five steps between sites, and to verify this computation with direct measurements of pressure differences. This comparison shows typical pressure mismatches for a single 500–600 m step of 20–30 Pa, equivalent to 2–3 mm of water.

Although we find that density consistently plays a significant role in explaining the mea-

sured pressure differences, it is velocity that is responsible for most of the variability at the timescales accessible to study. This means that resolving the velocity structure over the continental slope is critical to success in monitoring zonally-integrated transports. Density appears to play a relatively more important role at longer timescales, and may well become the dominant signal for interannual variability. It is also worth noting that the relevant density signal, near the sea floor, shows quite different variability from that at the same depth, but in open water above the deepest site RS6. Again, it remains to be seen whether this remains true at longer timescales, but it again emphasizes the importance of measuring right up to the boundary.

Unlike the direct pressure measurements, which suffer from significant long-term drifts, the indirect method using generalized hydrostatic balance is much more stable on long time scales. This makes it feasible to produce multi-year time series of the transport variability. The limiting factor for measurement accuracy appears to be the stability of salinity calibrations, which lead to density errors of about 0.002 kg m^{-3}, and hence pressure gradient errors of 20 Pa km^{-1}, an error that will be present in any measurement system which exploits thermal wind balance. Adding the effect of sampling and representation error, the stepping method leads to an accuracy equivalent to 0.82 Sv, for the zonally-integrated flow between approximately 1100 m and 3900 m, measured relative to 1100 m.

It is important to note that the measurements on the RS Line are not in themselves sufficient to calculate the complete overturning circulation at that latitude. What we have quantified in this paper are the zonally-integrated transports and their errors, below and relative to 1100 m, on the assumption that changes in the bottom pressure gradient on the eastern boundary are negligible in that depth range. Any density changes and varying currents at the ocean floor on the deep eastern continental slope will also contribute to the zonally-integrated meridional flow variability, as will any zonally-integrated current at the chosen reference depth. A measurement of the full geostrophic overturning would require the method to be applied using data over the full depth range at both eastern and western

boundaries.

With this paper, we introduce the RAPID-WAVE monitoring method and demonstrate that it works, and results in accuracy better than 1 Sv. Elsewhere (Elipot et al. 2012), we apply this method to demonstrate the degree to which coherent signals in the MOC can be seen across a range of latitudes. Future work will investigate the nature of that variability and its vertical structure in more detail.

Acknowledgments.

This work was supported by the UK Natural Environment Research Council as part of the RAPID-WATCH project. Thanks to the technology groups at BIO and NOC for their development and/or preparation of the moorings and instruments used in the field program; to the scientific personnel, officers and crew of the fall 2008 and 2009 CCGS Hudson expeditions for successful execution of the program; and to Yuri Geshelin, Ed Horne and Igor Yashayaev for advice and assistance with the observations and/or data processing. Conversations with Ric Williams were helpful in the development of this work.

APPENDIX

Appendix: Extension of the stepping method for complex topography

Consider two measurements at $y = 0$, $x = x_1$ (in shallower water) and $y = 0$, $x = x_2$ (in deeper water). At these two points, we have measurements that tell us $\nabla_h p_b$, where ∇_h is the horizontal gradient and p_b is the bottom pressure. The question is how best to use these values to calculate the pressure difference between the two points. Obviously, this involves some assumption about the smoothness of the pressure gradient, otherwise (having no knowledge of the pressure gradient between the two measurement points) the interpolation would be impossible. Note that, throughout this appendix, we are assuming pressure values to be differences from a hydrostatically-consistent reference profile, and similarly for density values wherever they are multiplied by g (the values denoted p' and ρ' in the body of the paper), but we will drop the primes to avoid a clash of notation. In addition, throughout this Appendix, the coordinate system is assumed to be rotated so that it is aligned with the particular pair of moorings considered, so that both lie on $y = 0$. We neglect the small effect of the changes in f that are implied by this when the pair of moorings are not at the same latitude.

If we have no other knowledge, then the simplest assumption is that the pressure gradient varies linearly in x and y, equivalent to assuming a quadratic variation of p_b in x and y:

$$p_b = ax + bx^2 + cxy + fy + gy^2, \tag{A1}$$

which results in the components of the gradient

$$\frac{\partial p_b}{\partial x} = a + 2bx + cy, \qquad \frac{\partial p_b}{\partial y} = cx + f + 2gy \tag{A2}$$

We can then calculate the pressure difference as

$$\delta p_b = p_{b2} - p_{b1} = \int_{x_1}^{x_2} \nabla p_b \cdot d\mathbf{s} = \int_{x_1}^{x_2} \frac{\partial p_b}{\partial x} dx. \tag{A3}$$

Performing the integral, this gives

$$\delta p_b = (x_2 - x_1)a + (x_2^2 - x_1^2)b = (x_2 - x_1)[a + b(x_2 + x_1)]. \tag{A4}$$

Now, using an overline to represent the average of the two values at points x_1 and x_2, application of (A2) at these two points (with $y = 0$), allows us to write

$$\overline{\frac{\partial p_b}{\partial x}} = a + b(x_2 + x_1), \tag{A5}$$

so that (A4) can be expressed as

$$\delta p_b = (x_2 - x_1)\overline{\frac{\partial p_b}{\partial x}}. \tag{A6}$$

In other words, the assumption of quadratic variation in x and y leads to the intuitive result that the pressure difference is the difference in x multiplied by the average of the values of $\partial p_b/\partial x$ measured at the two points. This is the simplest form of the calculation, which should work in all cases as long as the spacing of the stations is small enough for the quadratic assumption to be valid.

For real station separations, it is possible for the topography between x_1 and x_2 to be quite complicated, such that it cannot be well-approximated by a linear function. We expect that the flows are very strongly steered by topography, so complex topography would tend to lead to velocities that are not a linear function of x and y, thus reducing the accuracy of the interpolation. However, the strong topographic steering itself suggests a way of dealing with this.

Simple dynamical considerations (neglecting vertical velocity as a first approximation) lead to a flow that follows depth contours, and hence to a bottom pressure field which is purely a function of depth: $p_b = p_b(H)$. Within this approximation, the natural assumption of smoothness between the two measurement points, consistent with known pressure

gradients at those two points, is that pressure should be a quadratic function of H:

$$p_b = a + bH + cH^2, \tag{A7}$$

which leads to

$$\delta p_b = b(H_2 - H_1) + c(H_2^2 - H_1^2) = (H_2 - H_1)[b + c(H_2 + H_1)]. \tag{A8}$$

Writing $p'_b = dp_b/dH$, then we have $p'_{b1} = b + 2cH_1$ and $p'_{b2} = b + 2cH_2$ so, writing $\overline{p'} = (p'_{b1} + p'_{b2})/2 = b + c(H_1 + H_2)$, substitution into (A8) gives

$$\delta p_b = (H_2 - H_1)\overline{p'_b}. \tag{A9}$$

In this case, instead of using the component of the pressure gradient that lies along the line between points 1 and 2, the interpolation is performed as a function of H and involves the component of pressure gradient that is perpendicular to the depth contours at each point.

For the case in which the depth is a linear function of x and y and $p_b = p_b(H)$, (A6) and (A9) are exactly equivalent. In that case, $\partial H/\partial x$ and $\partial H/\partial y$ are constants, so that $(H_2 - H_1) = (\partial H/\partial x)(x_2 - x_1)$, and $p'_b = (\partial p_b/\partial x)/(\partial H/\partial x)$. In choosing between the different approaches, we are effectively making a choice between two approximations: is it better to assume that the points are so close together that the currents vary only linearly between them, or to assume that the spatially coherent part of the flow is purely along depth contours? For a flow that is strongly steered by topography, we would expect the second assumption to be better, although for closely-spaced stations there should be very little difference.

In order to apply these approximations, we first have to relate the quantities in the formulae, $\partial p_b/\partial x$ and p'_b, to the measured quantities, bottom density ρ and bottom velocity $\mathbf{u}$. Substituting geostrophic and hydrostatic balance into (A6), together with the matching assumption of constant slope, we obtain a formula for the pressure difference ignoring topographic steering, in terms of measured quantities:

$$\delta p = (x_2 - x_1)\overline{\rho f v} + (H_2 - H_1)\overline{\rho g}, \tag{A10}$$

where the overline, as usual, represents the average of the values at stations 1 and 2.

For the case assuming dominance of topographic steering, using the generalized hydrostatic balance (13), we have

$$p' = \frac{\rho f u_L}{H_s} + g\rho, \tag{A11}$$

where H_s is the (positive) gradient of H in the downslope direction, and u_L is velocity along the slope with deep water to the right.

Now, substituting (A11) into (A9) gives a formula for the pressure difference with topographic steering, in terms of measured quantities:

$$\delta p = (H_2 - H_1)\left(\overline{g\rho} + \overline{\left[\frac{\rho f u_L}{H_s}\right]}\right). \tag{A12}$$

Finally, there is a possible way of combining the best qualities of the two methods, i.e. using the knowledge that the primary pressure field is a function of depth, but without throwing away the information about differences from that primary pressure field which is available from the measurements in the form of the observed velocity perpendicular to depth contours. Whether this is an improvement over the assumption that $p_b = p_b(H)$ depends on the extent to which violations of this assumption are geostrophic and coherent over the required length scales. If the flow perpendicular to the depth contours is not geostrophic, or if it varies on very short length scales, then the "correction" suggested here will add noise to the estimate of pressure difference, rather than improving it.

Consider the situation shown in Fig. 12, in which the observations are at x_1 and x_2, and the line $\alpha\beta$ is the line of steepest descent between the depth contours on which the observations are made. In this situation, we could think of using p'_b to calculate the pressure difference between α and β, but using the velocity component normal to the depth contours to calculate the pressure differences between x_1 and α, and between β and x_2.

Using geostrophy, the pressure difference between x_1 and α is

$$p_{b\alpha} - p_{b1} = -s_1(\rho f u_D)_1, \tag{A13}$$

where u_D is the flow component perpendicular to the local depth contour (positive is toward deep water), and s_1 is the distance along the depth contour from x_1 to α (the positive direction is with deep water to the right). Similarly, on the deeper contour,

$$p_{b2} - p_{b\beta} = -s_2(\rho f u_D)_2, \tag{A14}$$

with s_2 the distance along the H_2 depth contour from β to x_2.

Using the assumption that p_b is a smooth function of H along $\alpha\beta$, we can use (A12) to write

$$p_{b\beta} - p_{b\alpha} = (H_2 - H_1)\left(\overline{g\rho} + \overline{\left[\frac{\rho f u_L}{H_s}\right]}\right) \tag{A15}$$

Choosing $s_1 = s_2 = S/2$, the sum of (A13)–(A15) then leads to

$$\delta p_b = (H_2 - H_1)\left(\overline{g\rho} + \overline{\left[\frac{\rho f u_L}{H_s}\right]}\right) - S\overline{[\rho f u_D]}, \tag{A16}$$

where the final term involving S represents the correction that should improve on the assumption $p = p(H)$.

In the case where H is a linear function of x and y, all H contours are parallel and are oriented at a constant angle θ (say) to the positive x direction, and $\alpha\beta$ becomes a straight line of length D (say). Then we can write $D = \delta x \sin\theta$ and $S = \delta x \cos\theta$, together with $(H_2 - H_1)/H_s) = D$. Substituting these values then gives

$$\delta p_b = (H_2 - H_1)g\overline{\rho} + \delta x \sin\theta\overline{[(\rho f u_L)]} - \delta x \cos\theta\overline{[(\rho f u_D)]}. \tag{A17}$$

Noting further that $v = -u_D \cos\theta + u_L \sin\theta$, and that $H_2 - H_1 = (\partial H/\partial x)\delta x$, this becomes

$$\delta p_b = \delta x\left[\overline{g\rho}\frac{\partial H}{\partial x} + \overline{\rho f v}\right], \tag{A18}$$

which, for constant $\partial H/\partial x$, is precisely equation (A10), derived by assuming that the velocities are linear functions of x and y.

Thus, in (A16), we have an equation that both accounts for complex topography where it occurs (by using the assumption that pressure is approximately a quadratic function of

depth), and reduces to the relation derived from the conventional assumption that velocities are linear functions of x and y in regions where H is a linear function of x and y.

In the paper, we refer to the simple method of (A10) as Method 1, the method that assumes dominance of topographic steering given by (A12) as Method 2, and the combined method of (A16) as Method 2e. For Method 2e we need an estimate of the along-slope offset S. This is chosen based on the offsets between lines of steepest descent illustrated in Fig. 6. For each instrument pair there are two such offsets, one at the depth of each instrument. The average of the two is used to define S, except in the cases involving RS5, for which no estimate of downslope velocity is available. In the latter cases, we use asymmetrical calculations with s_1 or s_2 set to zero, as appropriate. An alternative of using the value of S that produces the best fit between pressure differences was also tried, but in no case did it give a significantly better result than that found by other methods. The derived distances S are listed in Table 4.

REFERENCES

Bingham, R. J. and C. W. Hughes, 2008: Determining North Atlantic meridional transport variability from pressure on the western boundary: a model investigation. *J. Geophys. Res.*, **113 (C9)**, C09008, doi:10.1029/2007JC004679.

Elipot, S., C. W. Hughes, S. C. Olhede, and J. M. Toole, 2012: Coherence of western boundary pressure at the RAPID WAVE array: boundary wave adjustments or deep western boundary current advection? *J. Phys. Oceanogr.*, submitted, available at ftp://ftp.pol.ac.uk/pub/general/ship/manuscripts/Elipot2012a_rev.pdf.

Hughes, C. W. and B. A. de Cuevas, 2001: Why western boundary currents in realistic oceans are inviscid: a link between form stress and bottom pressure torques. *J. Phys. Oceanogr.*, **31 (10)**, 2871–2885.

Johns, W. E., L. M. Beal, M. O. Baringer, J. R. Molina, S. A. Cunningham, T. Kanzow, and D. Rayner, 2008: Variability of shallow and deep western boundary currents off the Bahamas during 2004-05: Results from the 26°N RAPID-MOC Array. *J. Phys. Oceanogr.*, **38 (3)**, 605–623, doi:10.1175/2007JPO3791.1.

Kanzow, T., H. L. Johnson, D. P. Marshall, S. A. Cunningham, J. J.-M. Hirschi, A. Mujahid, H. L. Bryden, and W. E. Johns, 2009: Basinwide integrated volume transports in an eddy-filled ocean. *J. Phys. Oceanogr.*, **39 (12)**, 3091–3110, doi:10.1175/2009JPO4185.1.

Kanzow, T., U. Send, W. Zenk, A. D. Chave, and M. Rhein, 2006: Monitoring the integrated deep meridional flow in the tropical North Atlantic: Long-term performance of a geostrophic array. *Deep Sea Research Part I: Oceanographic Research Papers*, **53 (3)**, 528–546.

808 Loder, J. W., C. G. Hannah, B. D. Petrie, and E. A. Gonzalez, 2003: Hydrographic and
809 transport variability on the Halifax section. *J. Geophys. Res.*, **108 (C11)**, 8003, doi:
810 10.1029/2002JC001267.

811 Lozovatsky, I. D. and S. M. Shapovalov, 2012: Thickness of the mixed bottom layer in the
812 northern Atlantic. *Oceanology*, **52 (4)**, 447–452, doi:10.1134/S0001437012010134.

813 Marsh, R., B. A. de Cuevas, A. C. Coward, J. Jacquin, J. J.-M. Hirschi, Y. Aksenov, A. J. G.
814 Nurser, and S. A. Josey, 2009: Recent changes in the North Atlantic circulation simulated
815 with eddy-permitting and eddy-resolving ocean models. *Ocean Modelling*, **28 (4)**, 226–239,
816 doi:10.1016/j.ocemod.2009.02.007.

817 Rayner, D., et al., 2011: Monitoring the Atlantic meridional overturning circulation. *Deep-*
818 *Sea Res. II*, **58 (17–18)**, 1744–1753, doi:10.1016/j.dsr2.2010.10.056.

819 Schott, F. A., J. Fischer, M. Dengler, and R. Zantopp, 2006: Variability of the deep western
820 boundary current east of the Grand Banks. *Geophys. Res. Lett.*, **33 (21)**, L21S07, doi:
821 10.1029/2006GL026563.

822 Send, U., M. Lankhorst, and T. Kanzow, 2011: Observation of decadal change in the Atlantic
823 meridional overturning circulation using 10 years of continuous transport data. *Geophys.*
824 *Res. Lett.*, **38**, L24606, doi:10.1029/2011GL049801.

825 Smith, W. H. F. and D. T. Sandwell, 1997: Global sea floor topography from satellite
826 altimetry and ship depth soundings. *Science*, **227 (5334)**, 1956–1962.

827 Toole, J., R. G. Curry, T. M. Joyce, M. McCartney, and B. Pena-Molino, 2011: Transport of
828 the North Atlantic deep western boundary current about 39°N, 70°W: 2004–2008. *Deep-*
829 *Sea Res. II*, **58 (17–18)**, 1768–1780, doi:10.1016/j.dsr2.2010.10.058.

830 Watts, D. R. and H. Kontoyiannis, 1990: Deep-ocean bottom pressure measurement:

831 Drift removal and performance. *J. Atmos. Oceanic Technol.*, **7 (2)**, 296–306, doi:
832 10.1175/1520-0426(1990)007⟨0296:DOBPMD⟩2.0.CO;2.

833 Wunsch, C., 2008: Mass and volume transport variability in an eddy-filled ocean. *Nature*
834 *Geoscience*, **1 (3)**, 165–168, doi:10.1038/ngeo126.

List of Tables

TABLE 1. Summary of the Rapid-Scotian line deployment. In the water depth column, the figures in parentheses are linearly interpolated from Smith and Sandwell (1997) seafloor topography data at 1 min resolution, (version 13.1) but smoothed with a 20-point 2D Gaussian window.

Mooring site	Location	Measured water depth (m)	BPR & μCAT records (days)	ADCP velocity records (days)
RS1	42°50.95'N, 61°37.85'W	1114 (1176)	359.1	359.5
RS2	42°44.26'N, 61°34.61'W	1701 (1771)	359.3	269.2
RS3	42°39.50'N, 61°27.70'W	2290 (2293)	359.7	360
RS4	42°33.35'N, 61°22.14'W	2784 (2766)	360.5	310.3
RS5	42°23.56'N, 61°16.57'W	3427 (3427)	361.2	NA
RS6	42°09.81'N, 61°04.22'W	3882 (3916)	361.5	283.1

TABLE 2. Skill (fraction of variance in directly-measured pressure difference explained by reconstructions, see (16)) for reconstructions based on density only (ρ-skill), velocity only (v-skill), and density and velocity, using Method 1, Method 2, and Method 2e. The final column shows the residual standard error using the full reconstruction, in Pa. Pairs for which data are complete with no known errors are marked in bold.

Pair	Method	ρ-skill	v-skill	Skill	Error (Pa)
RS1,2	1	-0.25	0.62	0.84	16.68
	2	-0.25	0.63	0.84	16.73
	2e			0.83	16.85
RS2,4	1	0.07	0.69	0.89	31.25
	2	0.07	0.69	0.90	30.42
	2e			0.89	31.83
RS2,3	1	0.04	0.55	0.76	27.40
	2	0.04	0.56	0.77	26.87
	2e			0.75	27.83
RS3,4	1	0.08	0.62	0.79	22.37
	2	0.08	0.60	0.78	22.95
	2e			0.76	23.82
RS4,5	1	0.12	0.62	0.68	36.13
	2	0.12	0.60	0.66	37.27
	2e			0.66	37.73
RS5,6	1	-0.02	0.59	0.58	76.84
	2	-0.02	0.35	0.39	92.79
	2e			0.45	87.61

TABLE 3. Statistics of reconstruction by Method 1 and Method 2 for pairs of mooring from RS1 to the other moorings. Pairs for which data are complete with no known errors are marked in bold.

Pair	Method	Skill	Error (Pa)
RS1,2	1	0.84	16.68
	2	0.84	16.73
RS1,3	1	0.85	35.79
	2	0.85	35.27
RS1,4	1	0.92	36.77
	2	0.92	35.86
RS1,5	1	0.90	49.64
	2	0.90	49.90
RS1,6	1	0.69	100.24
	2	0.64	108.54

TABLE 4. Distance parameter S used for Method 2e, as estimated from topography.

Pair	S (m)
RS1,2	839
RS2,4	9498
RS2,3	6713
RS3,4	6973
RS4,5	4032
RS5,6	7404

List of Figures

6 Grey lines: depth contours at 500 meters interval from Smith and Sandwell (1997) topography version 13.1. Thin black lines: same contours smoothed by a two dimensional Gaussian window of 20′ radius. Thick black lines: smoothed depth contours at the depths of the moorings RS1, RS2, RS3, RS4 and RS6. The path RS1 to β_2 (dashed line) is the steepest descent from RS1 to the depth contour of RS2. The path RS2 to α_1 is the steepest ascent from RS2 to the depth contour of RS1, and so on (see text). Variance ellipses and their major axes are plotted for the vertically averaged velocity record low-passed below 1 cycle per day. 50

7 In-situ density anomalies calculated from MicroCAT records at moorings RS1 to RS6 (a) and from instruments on tall mooring RS6 (b). Arbitrary offsets of 0.05 kg m^{-3} between curves are applied for legibility. The bottom curve in a) is repeated as the bottom curve in b). Data are shown every 10 minutes (grey), and after applying a 1 cycle per day low pass filter (black). 51

8 a) Pressure anomaly differences RS2 minus RS1 as measured by BPR (thick grey), and (black) as reconstructed by Method 1 (see Appendix). The individual contributions to the reconstruction from velocity and density are shown with offsets. b) Squared coherence, and c) phase of cross-spectra of the different components of the reconstructed pressure difference versus that directly measured from BPRs. Color of curves matches those in a). In b) the horizontal dashed line indicates the 95% confidence level for coherence squared. In a), the time series have been bandpass filtered between 1 and 50-day periods. The cutoff frequencies are marked as vertical dashed lines in b) and c). 52

9 Plots as in Fig. 8, but for the pressure difference RS4 minus RS2. 53

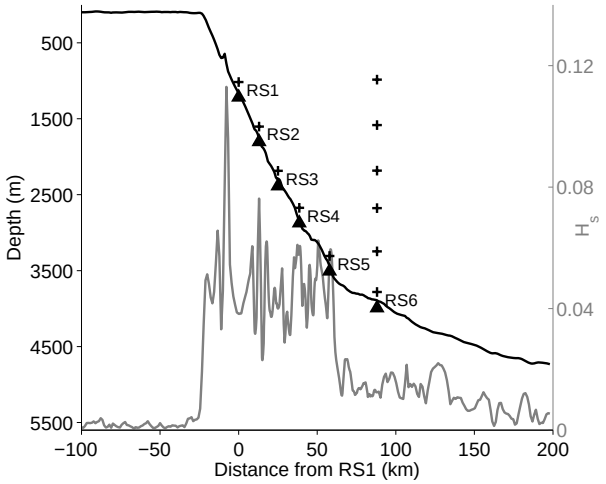

FIG. 1. Depth (black) and slope magnitude H_s (grey) as a function of distance along a great circle arc aligned with the RAPID-Scotian Line, using version 13.1 of the Smith and Sandwell (1997) topography dataset, at 1 minute resolution. Black triangles show the positions of the BPRs at RS1 to RS6, and pluses show the positions of MicroCATs. ADCPs are between the BPR and the (lowest) MicroCAT on each mooring

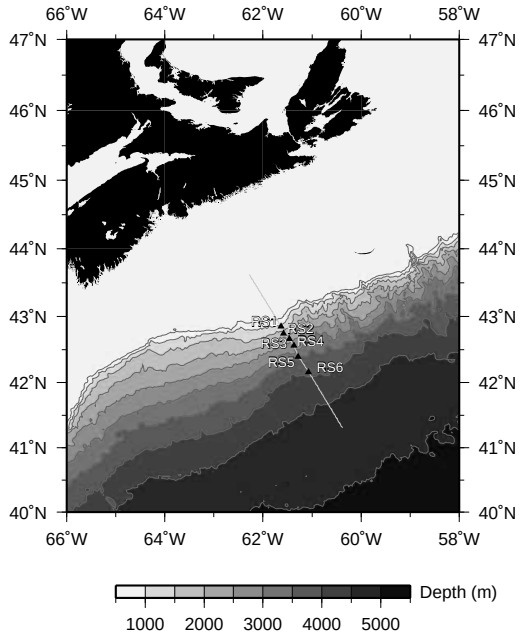

FIG. 2. The geography of the RAPID-Scotian Line, showing the position of instruments (black triangles), together with depth contours every 500 m, from version 13.1 of the Smith and Sandwell (1997) topography dataset, at 1 minute resolution.

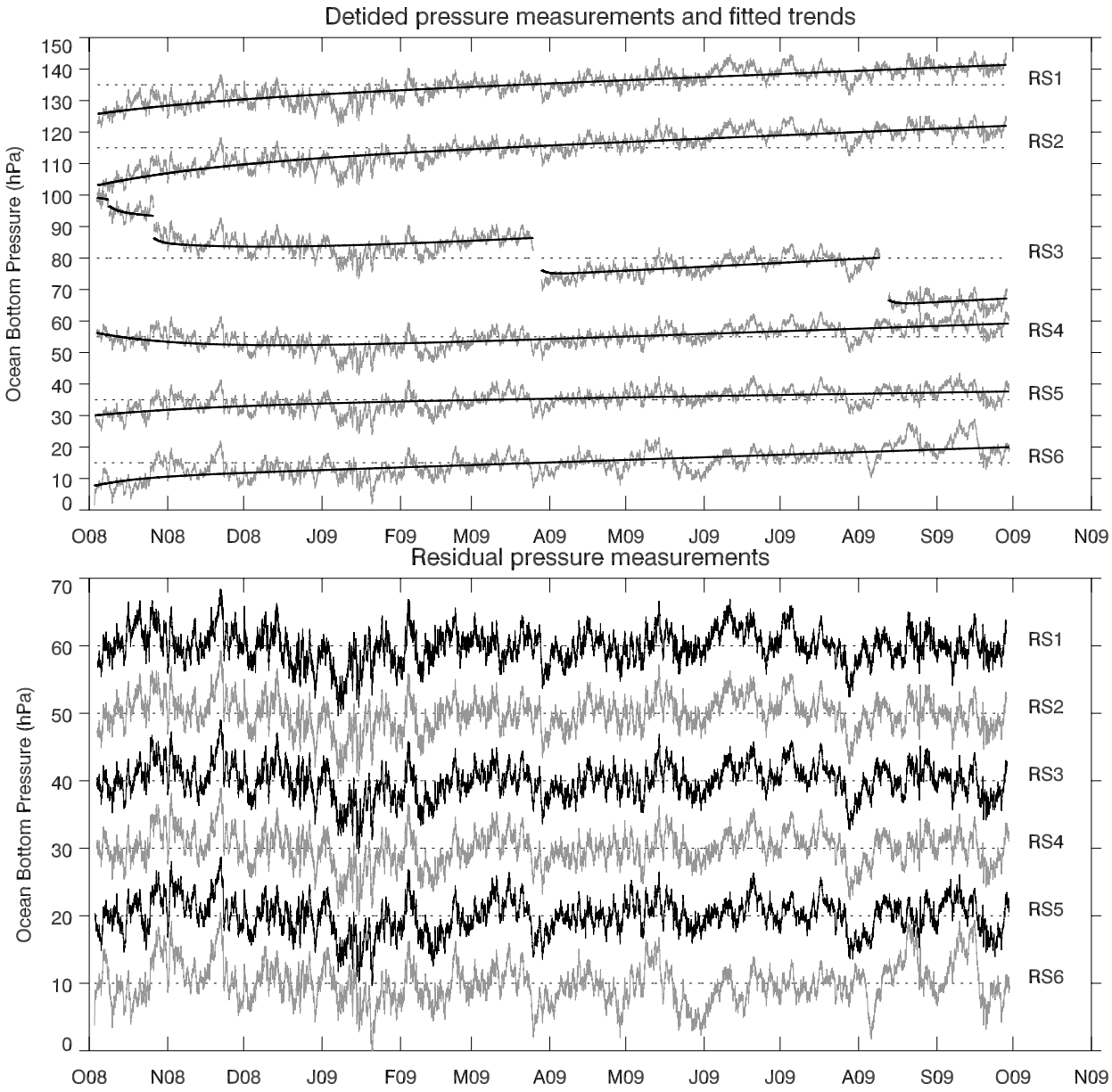

FIG. 3. Bottom pressure anomalies from the time mean, after subtraction of diurnal and higher-frequency tides. Top: Data before detrending, together with the fitted trend functions. Bottom: Residuals after detrending. Arbitrary vertical offsets have been applied for display purposes (dotted lines).

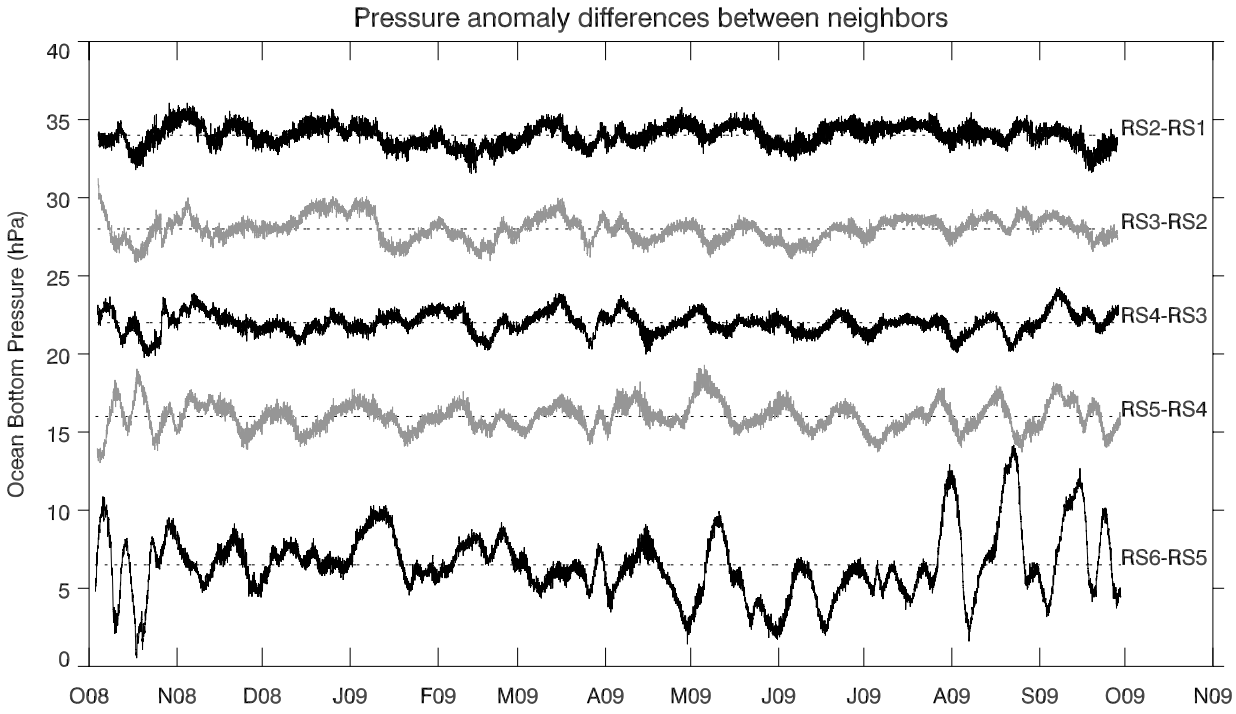

FIG. 4. Differences between neighboring pairs of bottom pressure residuals. Arbitrary mean values have been added for display purposes (dotted lines).

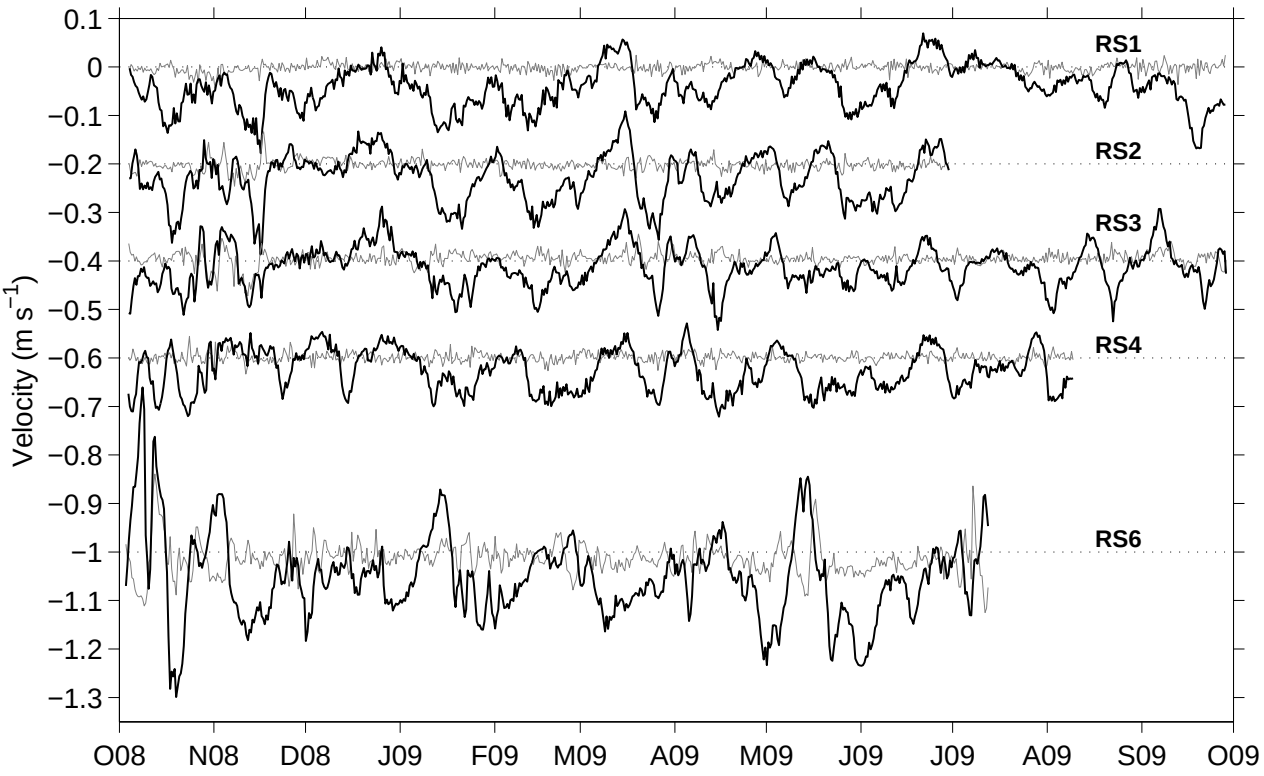

FIG. 5. Vertically-averaged near-bottom velocity records low-passed below 1 cycle per day. Black curves: first principal components at each site. Grey curves: second principal components. The orientations of the principal components at each site are shown on Fig. 6. The curves for RS2, RS3, RS4 and RS6 are offset by -0.2, -0.4, -0.6, and -1 m s^{-1} respectively.

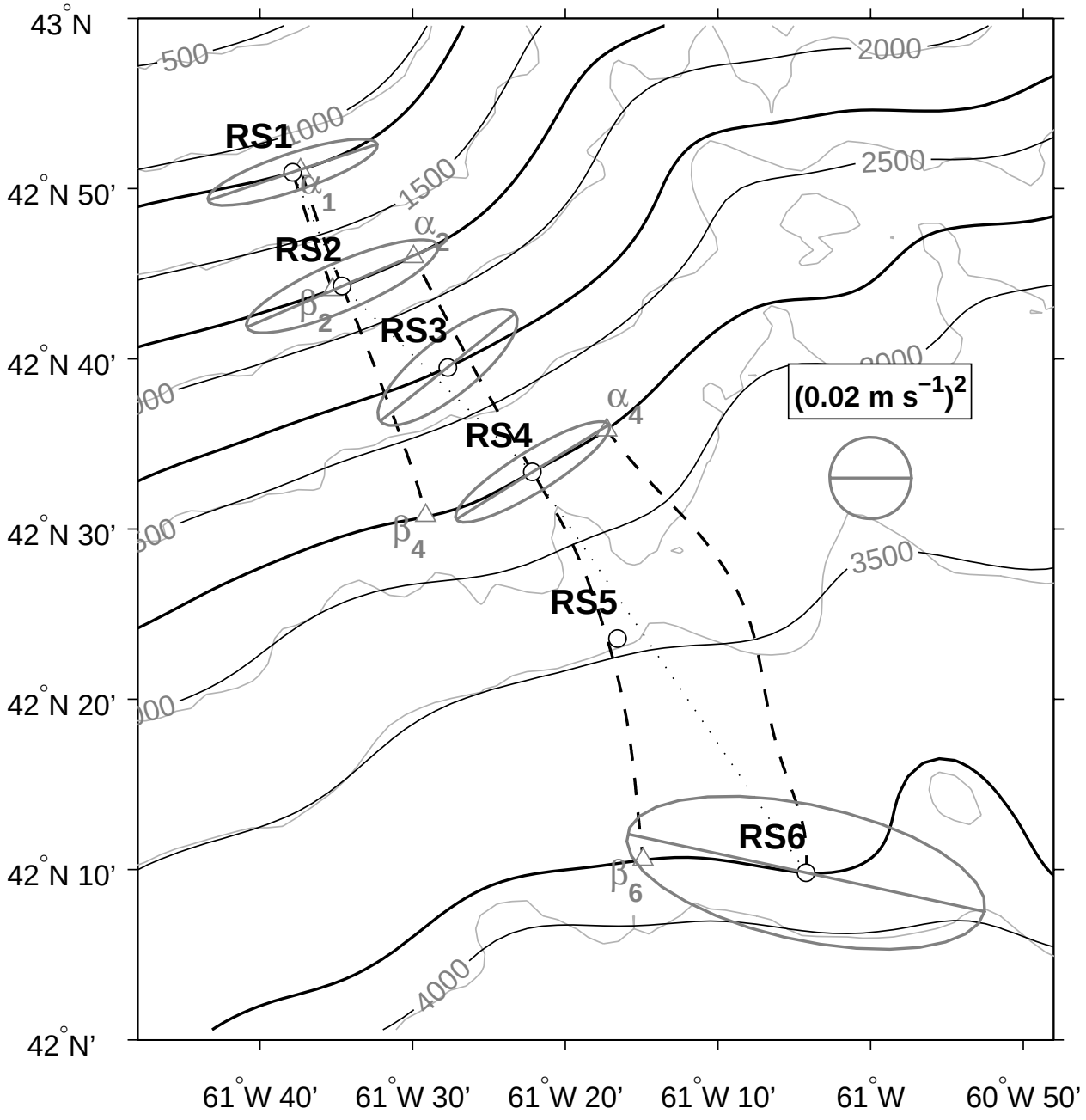

FIG. 6. Grey lines: depth contours at 500 meters interval from Smith and Sandwell (1997) topography version 13.1. Thin black lines: same contours smoothed by a two dimensional Gaussian window of 20′ radius. Thick black lines: smoothed depth contours at the depths of the moorings RS1, RS2, RS3, RS4 and RS6. The path RS1 to β_2 (dashed line) is the steepest descent from RS1 to the depth contour of RS2. The path RS2 to α_1 is the steepest ascent from RS2 to the depth contour of RS1, and so on (see text). Variance ellipses and their major axes are plotted for the vertically averaged velocity record low-passed below 1 cycle per day.

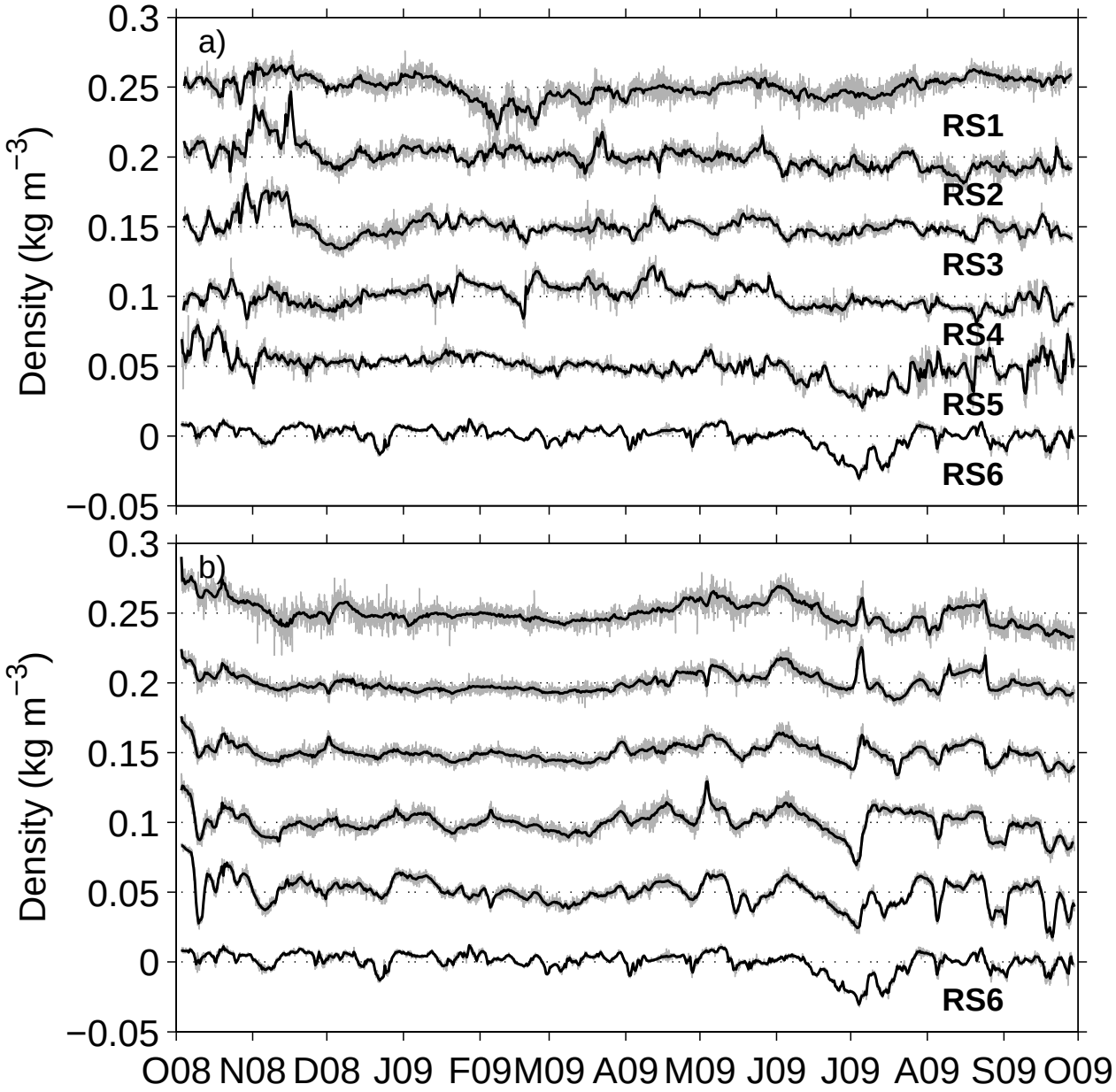

FIG. 7. In-situ density anomalies calculated from MicroCAT records at moorings RS1 to RS6 (a) and from instruments on tall mooring RS6 (b). Arbitrary offsets of 0.05 kg m^{-3} between curves are applied for legibility. The bottom curve in a) is repeated as the bottom curve in b). Data are shown every 10 minutes (grey), and after applying a 1 cycle per day low pass filter (black).

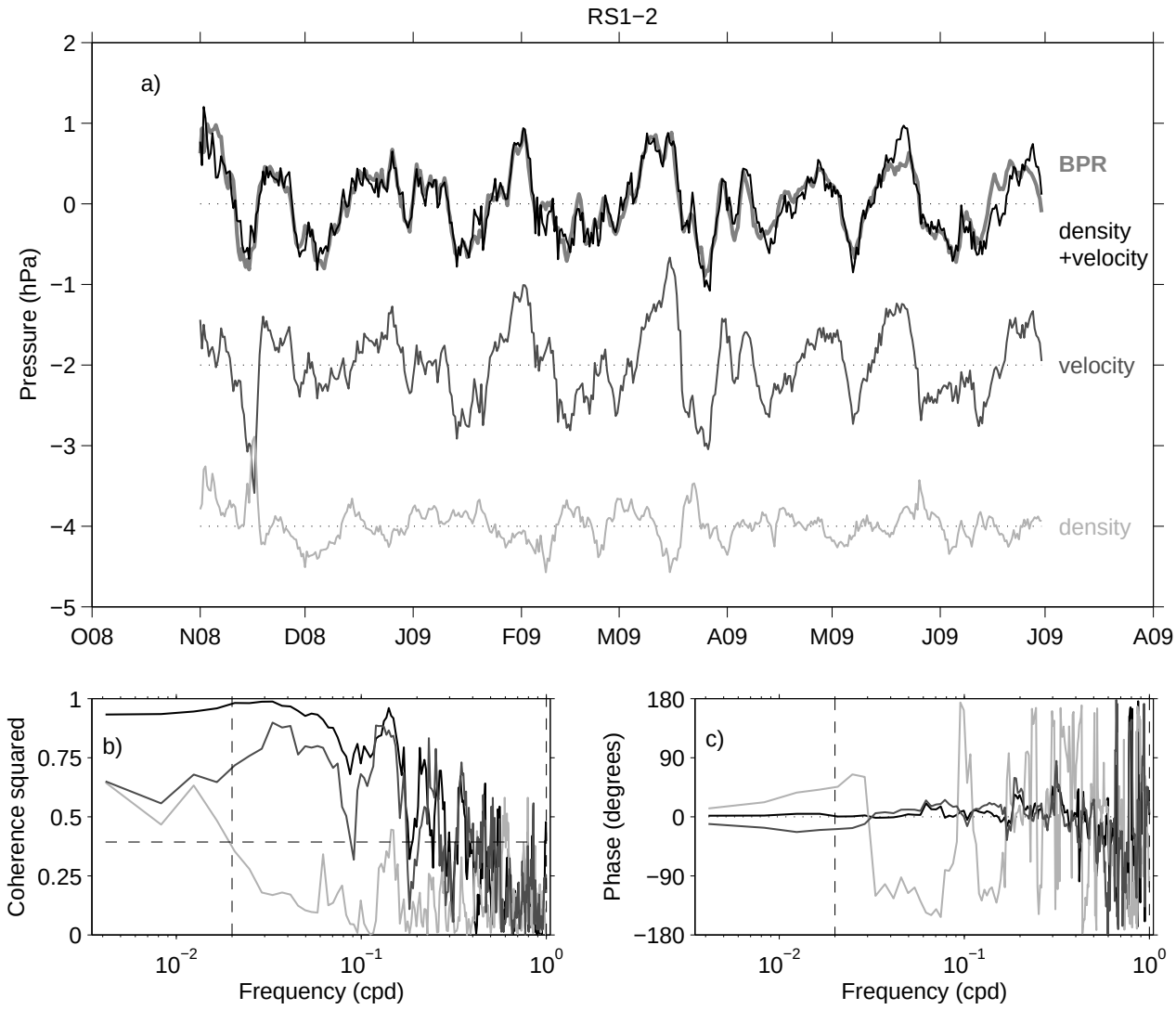

FIG. 8. a) Pressure anomaly differences RS2 minus RS1 as measured by BPR (thick grey), and (black) as reconstructed by Method 1 (see Appendix). The individual contributions to the reconstruction from velocity and density are shown with offsets. b) Squared coherence, and c) phase of cross-spectra of the different components of the reconstructed pressure difference versus that directly measured from BPRs. Color of curves matches those in a). In b) the horizontal dashed line indicates the 95% confidence level for coherence squared. In a), the time series have been bandpass filtered between 1 and 50-day periods. The cutoff frequencies are marked as vertical dashed lines in b) and c).

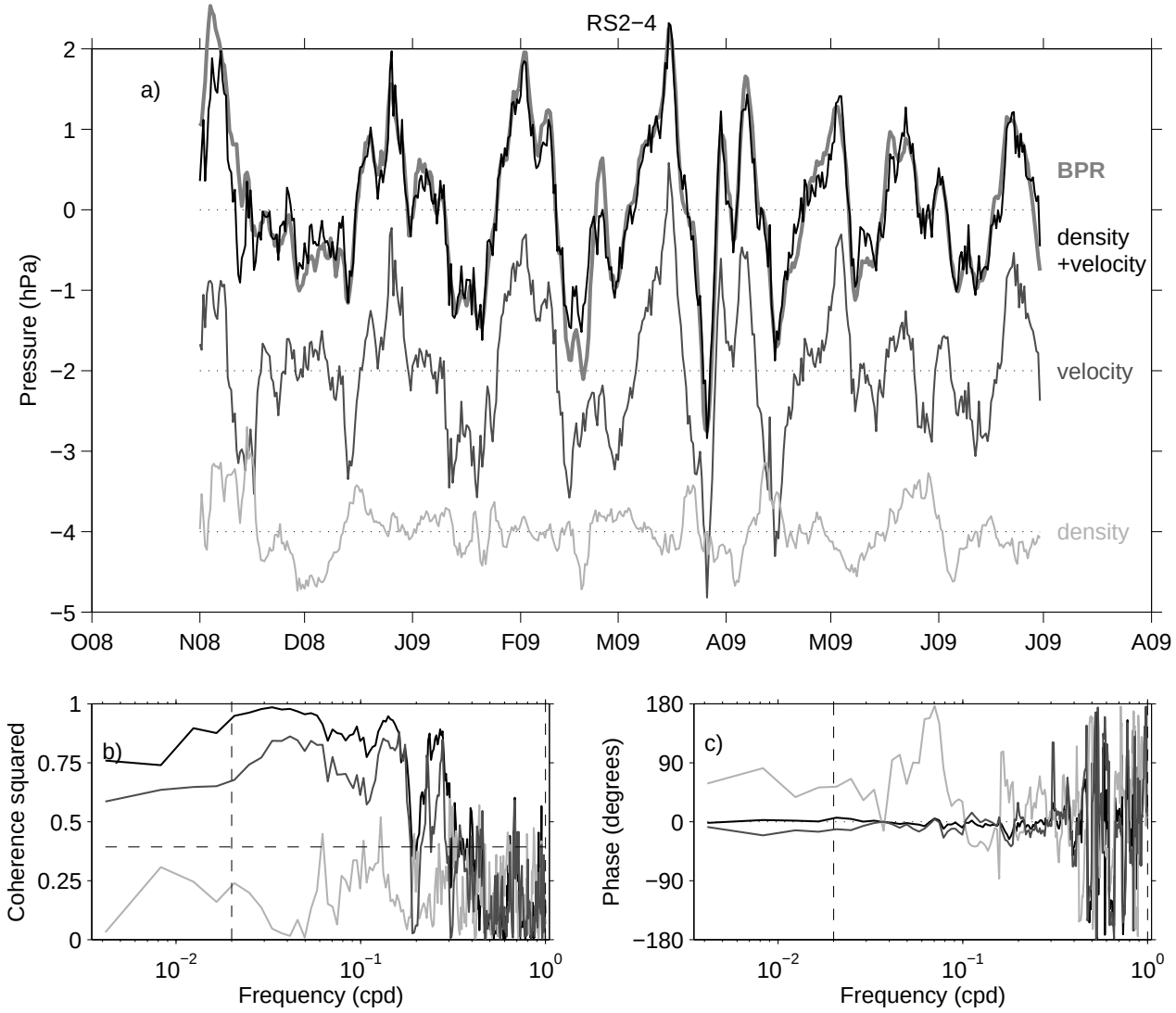

FIG. 9. Plots as in Fig. 8, but for the pressure difference RS4 minus RS2.

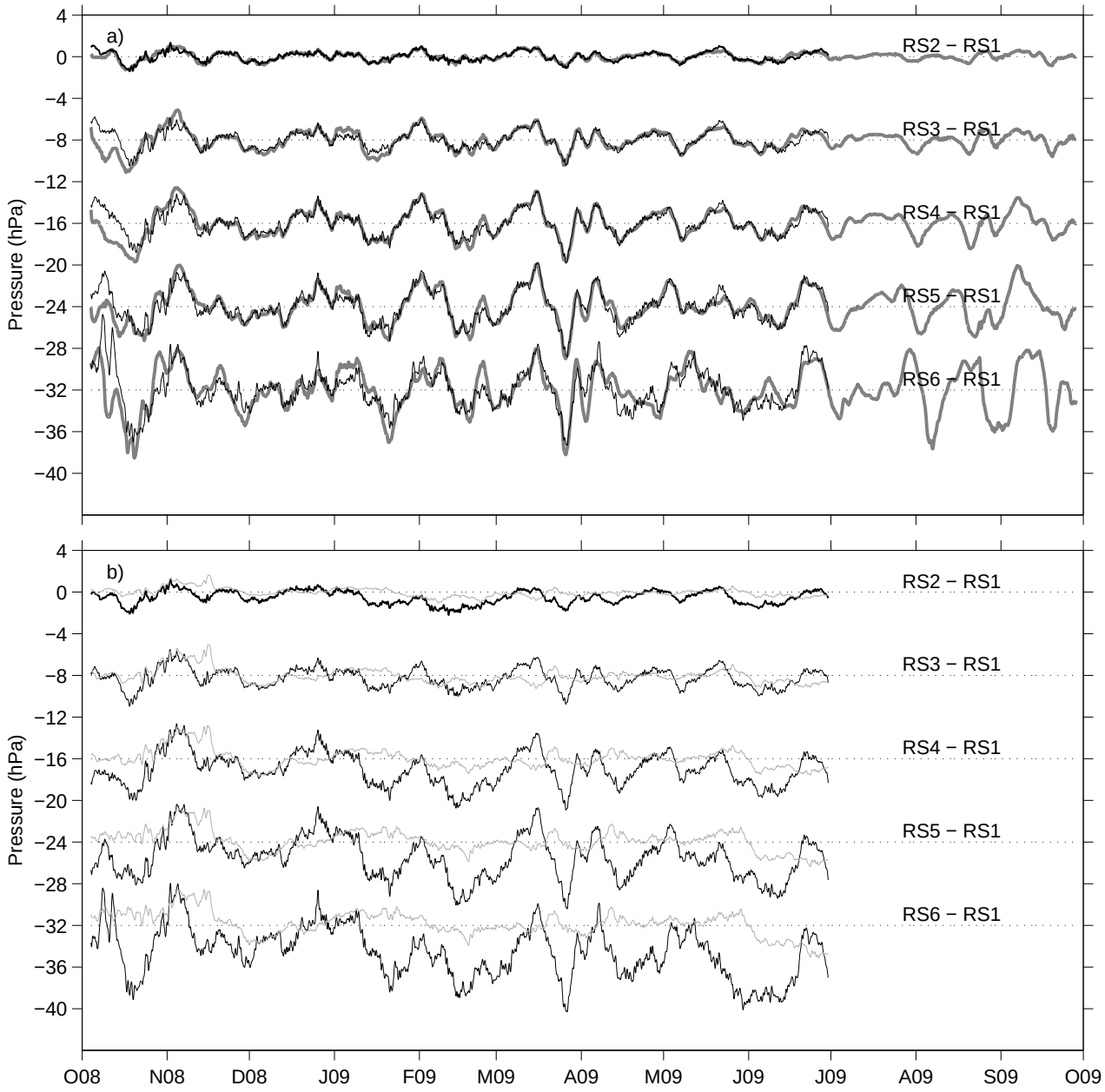

FIG. 10. a) Pressure differences for RS2, RS3, RS4, RS5, and RS6 minus RS1. All time series are bandpass filtered, passing periods of 1–50 days. Grey thick curves are from BPR data and thin black curves are from Method 1. Dotted lines show arbitrary offsets applied to the means. b) The same pressure differences from Method 1, but with a low-pass filter applied, passing all periods longer than 1 day. Black curves show the total pressure difference, and grey curves show the component due to density only.

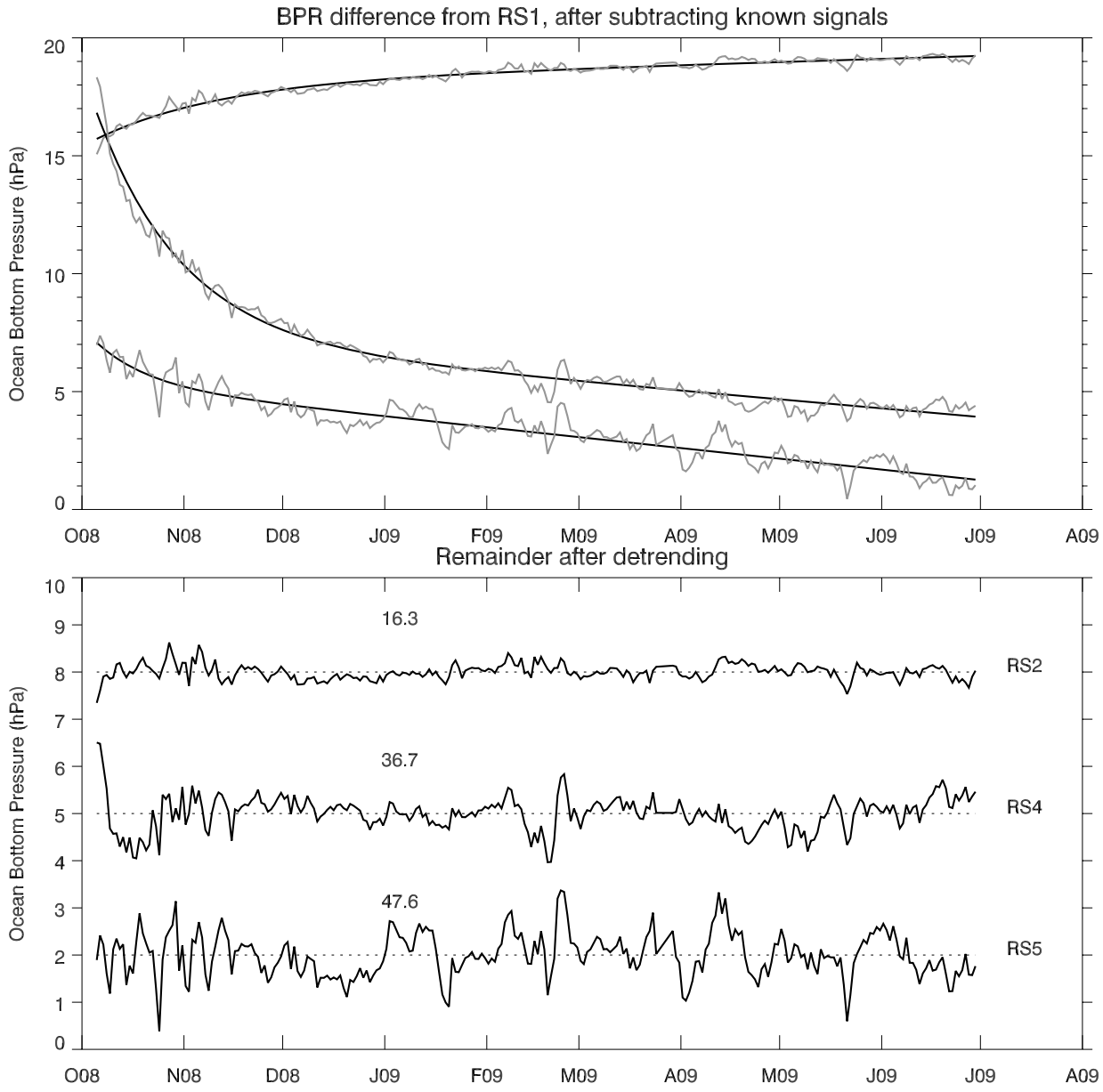

FIG. 11. Time series of pressure differences relative to RS1, as measured by BPRs at RS2, RS4 and RS5, following subtraction of the dynamical pressure signal reconstructed using the stepping method (Method 1). The top panel shows the complete time series with no detrending applied (grey), together with fitted exponential plus linear trends (black), with arbitrary vertical offsets (not shown). Bottom: residuals after subtracting the fitted trends (arbitrary mean values shown as dotted lines). The numbers above each curve are standard deviations in Pa. All curves represent daily mean values, following the removal of tides.

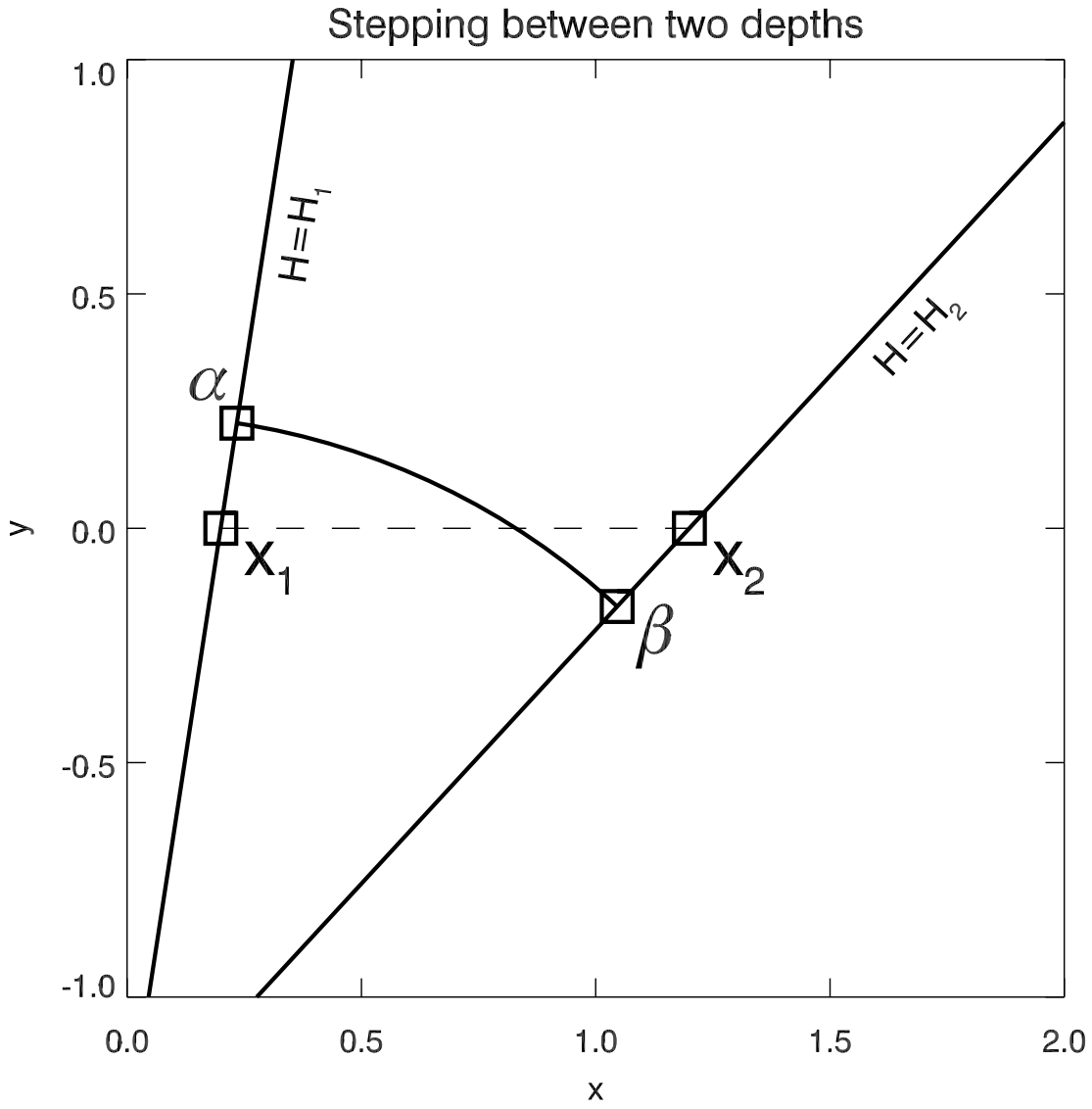

FIG. 12. Schematic of the geometry in a case with varying topographic gradient between the two observations.